BULETINUL
INSTITUTULUI
POLITEHNIC
DIN IAŞI

Tomul LIX (LXIII)

Fasc. 1

ŞTIINȚA ŞI INGINERIA MATERIALELOR

2013 **Editura POLITEHNIUM**

BULETINUL INSTITUTULUI POLITEHNIC DIN IAŞI
PUBLISHED BY
„GHEORGHE ASACHI” TECHNICAL UNIVERSITY OF IAŞI
Editorial Office: Bd. D. Mangeron 63, 700050, Iaşi, ROMANIA
Tel. 40-232-278683; Fax: 40-232 237666; e-mail: polytech@mail.tuiasi.ro

Editorial Board

President : Prof.dr.eng. **Ion Giurma**, Member of the Academy of Agricultural Sciences and Forest, *Rector* of the "Gheorghe Asachi" Technical University" of Iaşi

Editor-in -Chief : Prof.dr.eng. **Carmen Teodosiu,** *Vice-Rector* of the "Gheorghe Asachi" Technical University of Iaşi

Honorary Editors of the Bulletin: Prof.dr.eng. **Alfred Braier**
Prof.dr.eng. **Hugo Rosman**
Prof.dr.eng. **Mihail Voicu,** Corresponding Member of the Romanian Academy

Editors in Chief of the MATERIALS SCIENCE AND ENGINEERING *Section*

Assoc. Prof. Dr. Eng. **Iulian Ioniță**
Assoc. Prof. Dr. Eng. **Gheorghe Bădărău**
Prof. Dr. Eng. **Dan Gelu Găluşcă**
Prof. Dr. Eng. **Costică Bejinariu**

Honorary Editors: Prof. Dr. Eng. **Ion Hopulele,** Prof. Dr. Eng. **Ion Mălureanu**,
Prof. Dr. Eng. **Adrian Dima**
Associated Editor: Assoc. Prof.Dr. Eng. **Ioan Rusu**

Editorial Advisory Board

Prof.dr.eng. **Agustin Santana Lopez,** La Palmas de Gran Canaria University, (Spain)

Prof.dr.eng. **Mihai Susan,** Technical University “Gheorghe Asachi” from Iasi, (Romania

Prof.dr.eng. **Ioan Carcea,** Technical University “Gheorghe Asachi” from Iasi, (Romania

Prof.dr. **Duu-Jong Lee**, National Taiwan University of Science and Technology, (Taiwan)

Prof.dr.eng. **Shih-Hsuan Chiu**, National Taiwan University of Science and Technology, (Taiwan)

Prof.dr.eng. **Yuri A. Burennikov**, Vinnitsya National Technical University, (Ukraine)

Prof. dr. **Oronzio Manca**, Seconda Università degli Studi di Napoli (Italy)

Prof.dr.eng. **Julia Mirza Rosca**, La Palmas de Gran Canaria University, (Spain)

Prof.dr.eng. **Petrică Vizureanu,** Technical University “Gheorghe Asachi” from Iasi, (Romania

Assoc. Prof. **Shizutoshi Ando**, Tokyo University of Sciences, (Japan)

Prof.dr.eng. **Leandru-Gheorghe Bujoreanu,** Technical University “Gheorghe Asachi” from Iasi, (Romania)

Prof. dr. eng. **Constantin Baciu**, Technical University “Gheorghe Asachi” from Iasi, (Romania)

Dr. **Koichi Tsuchiya**, National Institute for Materials Science (Japan)

Dr.eng. **Burak Özkal**, Istanbul Technical University (Turkey)

Prof. dr. eng. **Vasile Cojocaru-Filipiuc**, Technical University “Gheorghe Asachi” from Iasi, (Romania)

Prof. dr. **Viorel Păun**, University “Politehnica” Bucharest, (Romania)

Prof.dr. **Maricel Agop**, Technical University “Gheorghe Asachi” from Iasi, (Romania)

Prof.dr.eng. **Sergiu Stanciu,** Technical University “Gheorghe Asachi” from Iasi, (Romania)

BULETINUL INSTITUTULUI POLITEHNIC DIN IAŞI
BULLETIN OF THE POLYTECHNIC INSTITUTE OF IAŞI
Tomul LIX (LXIII), Fasc. 1 2013

ŞTIINȚA ŞI INGINERIA MATERIALELOR

SUMAR

Pag.

DIANA-ANTONIA GHEORGHIU, TRAIAN MIHORDEA, COSTICĂ BEJINARIU şi ŞTEFAN LUCIAN TOMA, Studiul fractografic al ruperii imbinarilor WIG pe aliajul AlSi11 (engl. rez. rom.) 9

VASILE COJOCARU FILIPIUC, Temperatura de formare a nucleilor de grafit în fonta turnată, în condiții de echilibru termodinamic (engl. rez. rom.) 17

VASILE COJOCARU FILIPIUC, Producerea de fontă cu grafit coral (engl. rez. rom.) 29

VASILE COJOCARU FILIPIUC, Ipoteză asupra mecanismului formării grafitului nodular utilizând ca modificator magneziul (engl. rez. rom.) 39

MARIA BACIU, ELENA-RALUCA BACIU, IRINA GRĂDINARU şi NORINA-CONSUELA FORNA, Considerații privind metalurgia fizică a aliajelor pe bază de Ti destinate proteticii dentare (engl. rez. rom.) 49

GELU BARBU, Studii privind influența vibrațiilor asupra unui aliaj cu 95% Al, 4.5% Cu, 0.14% Fe, 0.28% Si (engl. rez. rom.) 55

VASILE BAHRIN, Considerații asupra limitatoarelor supraconductoare (engl. rez. rom.) 63

V. STRUTINSKIY, Y. BURENNIKOV şi L. KOZLOV, Optimizarea parametrilor sistemului hidraulic mecatronic prin metoda algoritmului generic (engl. rez. rom.) 69

BULETINUL INSTITUTULUI POLITEHNIC DIN IAŞI
BULLETIN OF THE POLYTECHNIC INSTITUTE OF IAŞI
Tomul LIX (LXIII), Fasc. 1 2013

MATERIALS SCIENCE AND ENGINEERING

CONTENTS

Pp.

DIANA-ANTONIA GHEORGHIU, TRAIAN MIHORDEA, COSTICĂ BEJINARIU and ŞTEFAN LUCIAN TOMA, Fractographic Study of the Fractured Surfaces in Alsi11 Joints Accomplished by Tig Welding (English, Romanian summary) 9

VASILE COJOCARU FILIPIUC, Temperature of Graphite Nuclei Formation in Cast Irons, in Thermodynamic Equilibrium Conditions (English, Romanian summary) 17

VASILE COJOCARU FILIPIUC, Production of Coral-Like Graphite Cast Iron (English, Romanian summary) 29

VASILE COJOCARU FILIPIUC, Hypothese on the Mechanism of Nodular Graphite Formation in Magnesium (English, Romanian summary). 39

MARIA BACIU, ELENA-RALUCA BACIU, IRINA GRĂDINARU and NORINA-CONSUELA FORNA, Considerations Regarding the Physical Metallurgy of Ti-Based Alloys for Dental Prosthetics (English, Romanian summary) 49

GELU BARBU, Study Regarding the Influence of Vibrations on the Alloy 95% Al, 4.5% Cu, 0.14% Fe, 0.28% Si (English, Romanian summary) 55

VASILE BAHRIN, Considerations on Superconducting Limit Switches (English, Romanian summary) 63

V. STRUTINSKIY, Y. BURENNIKOV and L. KOZLOV, Optimization of the Mechatronic Hydraulic System Parameters by the Method of Genetic Algorithm (English, Romanian summary) 69

BULETINUL INSTITUTULUI POLITEHNIC DIN IAŞI
Publicat de
Universitatea Tehnică „Gheorghe Asachi” din Iaşi
Tomul LIX (LXIII), Fasc. 1, 2013
Secţia
ŞTIINŢA ŞI INGINERIA MATERIALELOR

FRACTOGRAPHIC STUDY OF THE FRACTURED SURFACES IN ALSI11 JOINTS ACCOMPLISHED BY TIG WELDING

BY

**DIANA-ANTONIA GHEORGHIU*, TRAIAN MIHORDEA,
COSTICĂ BEJINARIU and ŞTEFAN LUCIAN TOMA**

“Gheorghe Asachi” Technical University of Iaşi
Faculty of Material Science and Engineering

Received: February 28, 2012
Accepted for publication: March 7, 2012

Abstract: Aluminum and its alloys plays a major role our days into the economic life. Welding aluminum alloys is a current practice, as it is for many other metallic materials. Wrought aluminum alloys are frequently welded as their weldability is deeply investigated, but the cast ones do not enjoy the same interest. Among the cast grades AlSi alloys are almost neglected. The present work investigates some peculiarities for the fracture surfaces resulted after the tensile test of some TIG welded samples with base material AlSi11 alloy. It is proved that the fracture surfaces are very much alike the base material fracture and the main changes are related to the weld process discontinuities, namely pores.

Keywords: aluminum-silicon alloy; base material; porosity; GTAW process.

1. Introduction

Aluminum physical properties are well known: low density, high thermal and electric conductivity, high formability, good corrosion resistance and so on. In the automotive industry, naval construction and in the aerospace appliance the low density associated with its good strength make aluminum and

---

*Corresponding author: *e-mail*: dagheorg@tuiasi.ro its alloys an excellent material choice. This association provides a better weight to strength ratio and by consequence a better fuel consumption with good effects on both the economic and environment aspect.

As a result, many alloys grade were conceived and put into service. It can be said that there are hundreds of them, mostly polyelemental alloys. These are classified on the basis of the main alloying element into nine groups. The chemical composition and the associated technological properties divide each of these groups in wrought alloys and castable alloys. Further, the strengthening mechanisms divide again the aluminum alloy family. There are five mechanisms that can be applied. These are grain size control, solid solution alloying, second phase formation, strain hardening (cold working) and precipitation or age hardening. It is obviously that some of them will act into the castable alloys and other will be effective into the wrought ones.

Weldability of the aluminum alloys is intensively studied relative to the wrought ones the cast ones have not enjoyed the same interest (Katsas *et al*., 2006).

From the as mentioned nine groups the fourth one includes aluminum – silicon alloys, designated for cast processing. The silicon content in standardized commercial cast aluminum silicon alloys is in the range of 5 to 23 wt%. The equilibrium diagram exhibits an eutectic point at 11.7% silicon (weight). The most frequently used compositions range about 1%Si to about 12%Si. Their structure consists from solid solution of Si into Al matrix (α-phase), and almost pure silicon, β-phase. Silicon precipitates are in fact almost pure silicon crystals. The crystals have different appearance: large, coarse into hypereutectic compositions, or fine, almost round shaped into eutectic or hypoeutectic ones. The properties of the metal are under the silicon content control.

The mechanical properties of cast aluminum-silicon alloys can be improved by cast technology and heat treatment processes that: increase the strength of soft matrix; decrease the brittle fracture risk in the polyphase regions; increase the degree of dispersion of the dendritic structure. These goals can be attempted through interfere solidification moment by modifying the alloy and/or by controlling the cooling rate.

Welding process will change the structure and by consequence the mechanical properties of the metal. It shall be seen if the fracture mode also differs.

2. Experimental Procedures

In order to investigate the weldability of the AlSi11 alloy samples with the 4 × 150 × 200 mm dimensions were prepared. The chemical composition of the base metal is shown in Table 1.

In the present paper GTAW procedure was used, a choice made in perfect agreement with the welding solutions in the actual practice. The process parameters in the experiment are summarized in Table 2.

Two different compositions of filler material were used, AlSi5 and AlSi12, that is a common filler metal for aluminum welds and a filler metal with almost the same composition than the base metal. The characteristics of the filler materials are shown in Table 3.

In order to accomplish the joint, the specimens have been welded from both sides, with the removal of the root weld pass.

Table 1

Chemical Composition of the Base Metal

Alloy group	Numerical symbol	Chemical composition, [%wt]					
		Si	Fe	Cu	Mn	Others	Al
AlSi11	EN AC-44000	11.7	0.478	0.507	0.186	0.829	Bal.

Table 2

Welding Parameters for GMAW Process

Phases	Is, [A]	d_{MA}, [mm]	$d_{el\ W}$, [mm]	v_s, [cm/min]	q, [L/min]	υ, [Hz]
Root pass	100	2.4	2.4	8.3	8	160
Upper passes	80	2.4	2.4	9.6	8	160

Is – welding current; d_{MA} – filler metal diameter; v_s – welding speed; q – gas flow; υ – frequency.

Table 3

Chemical Composition of the Filler Metal According to SR EN 573-3

Filler metal symbol	Chemical composition, [%]							
	Si	Fe	Cu	Mn	Mg	Zn	Others	Al
EN AW AlSi5(A)	4.5…6.0	0.6	0.3	0.15	0.2	0.1	0.15	Bal
EN AW AlSi12(A)	11…13	0.6	0.3	0.15	0.1	0.1	0.15	bal

From the welded part were cut samples for the tensile test. As the base material became from a cast part the samples for the strength test have a rectangular section of 4 × 5 mm, the gauge length was 25 mm, complying with the recommendations ISO 6892-1:2009.

For the base material (as cast) samples, the results were compared with the recommended mechanical characteristics for the cast aluminum alloys. The assumed maximum values for the part cast samples must equal or exceed 70% from the recommended tensile stress for cast alloys, as stipulated by SR EN 1706: 2000.

So, to assure a true solid comparison, samples from the base metal were also prepared. To test the joint itself as well as the welded metal, tensile test samples with a notch in the deposed metal were also prepared [2]. Sketches of both sample types are presented in Fig. 1. The tensile tests were accomplished on an Instron 3382 equipment. The failed surfaces were investigated by stereomicroscopy and further through a Tescan scanning electron microscope.

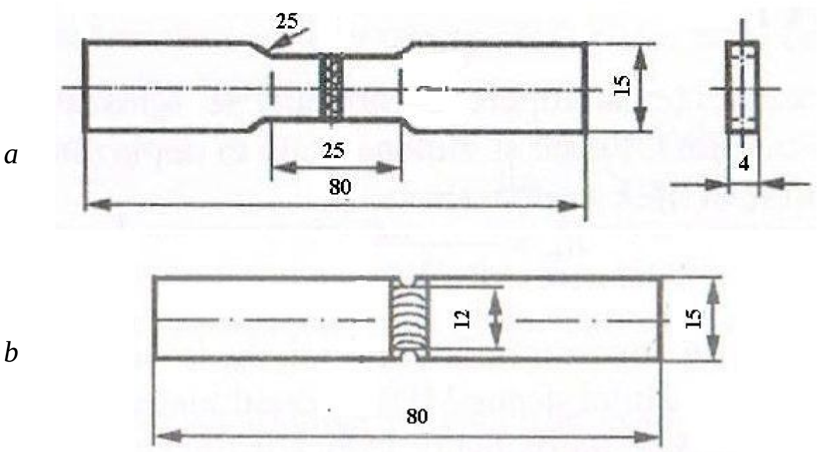

Fig. 1 – Tensile test samples: *a* – classic sample, for joint strength test; *b* – notched sample, for filler metal test.

3. Experimental Results

Because SR EN 1706: 2000 recommends for the tensile strength values that have been obtained in specific conditions, maximum values for ultimate tensile test and for tensile test at yielding were calculated, according to the same standard. In the whole experiment only one proof failed at a lower stress value than that recommended.

The tensile test reveals that welding AlSi11 alloy in the as mentioned conditions results in good strength joint, with strength values that equals or even exceeds the recommended values as well as the measured on the base material ones (Fig. 2). It must be highlight the fact that the failure occurs especially in the HAZ, or at least the fracture begins from there. Even the notched specimens failed in the HAZ.

Descriptions of the characteristic features of fracture surface are very important for establishing the dependence between the decohesion mechanism (dependent on physical and mechanical properties) and material microstructure (determined by chemical composition and production technology). Fractographic examination of metals can evaluate the cause of the failure by revealing material discontinuities internal cracks, porosity, inclusions and chemical or microstructure inhomogeneities and also can determine the decohesion mechanism by describing the characteristic morphological features of the fracture surface.

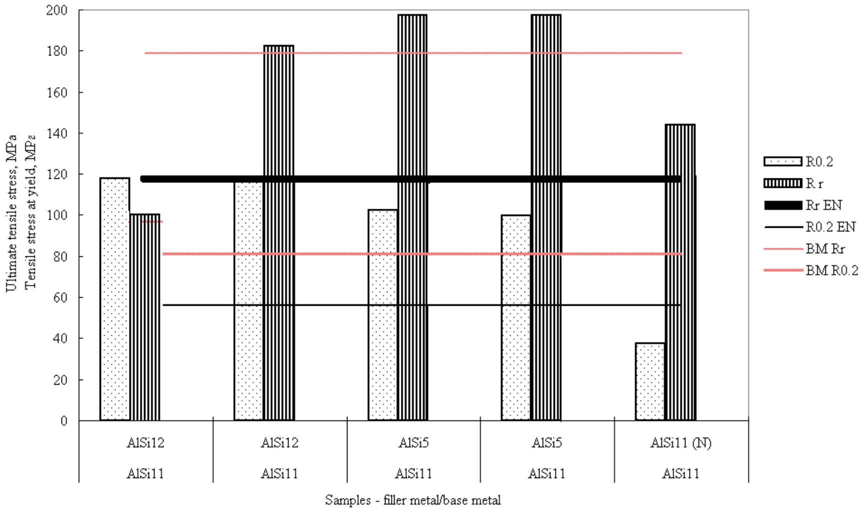

Fig. 2 – Tensile stress test results. Thin lines: values of the as determined values for the base metal; dark thick lines: calculated values for the base metal.

The failed surfaces of the base metal samples (Fig. 3), reveals a complex fracture profile, with a complex, irregular geometry. The surfaces are mainly smooth, with a lot of shiny little points with facet surfaces. It can be assumed that these are silicon crystals. Small pores and little cracks are also visible.

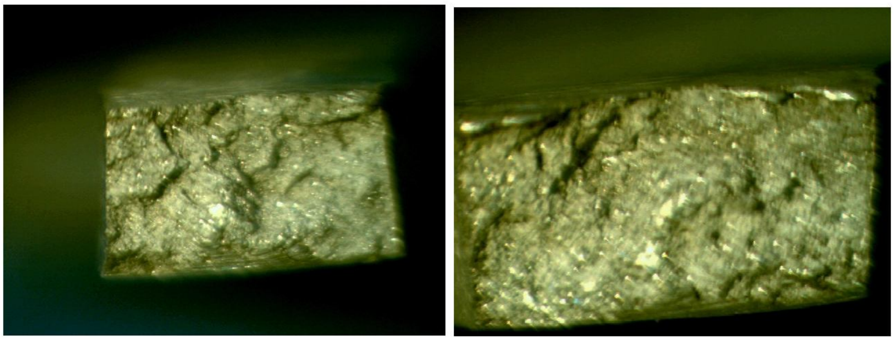
a *b*

Fig. 3 – Base material surfaces not welded: *a* – very irregular smooth surface; *b* – pores and cracks on the surface.

In the welded samples the failed surfaces are similar with those from the base material (Fig. 4). The pores dimensions mark a consistent growth.

In the weakest sample (Fig. 4), the surfaces are divided into three regions: a central zone, with a great amount of little pores but no crack. The side zones are different, with respect to the phase of the weld. The latest weld side exhibits rough porosity, while the first are very much like the base material.

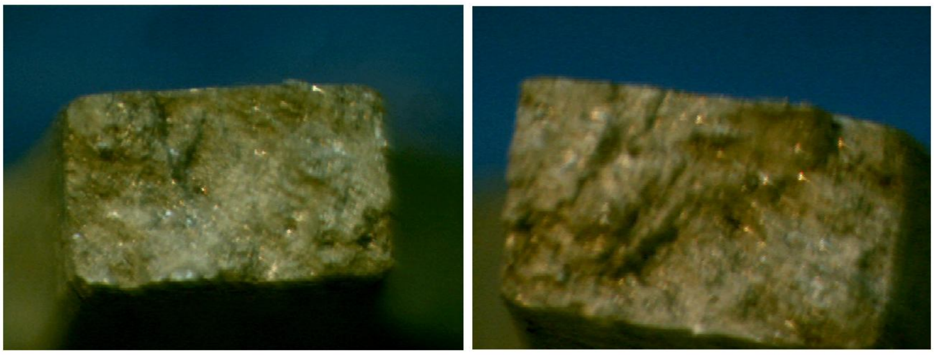

Fig. 4 – Fracture surface in welded samples: *a* – AlSi5 filler metal – transcrystalline fracture, surface very much alike the base metal; *b* – AlSi12 filler metal – coarse surface with massive pores and cracks.

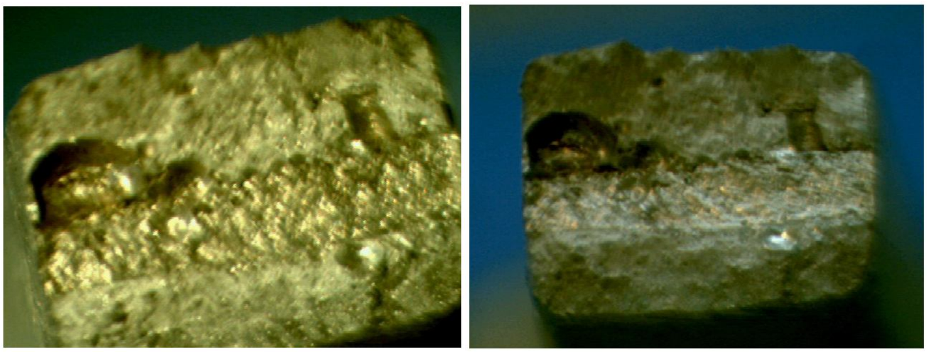

Fig. 5 – The sample with the poorest tensile test result: massive porosity.

Porosity is a problem confined to the weld metal. It arises from gas dissolved in the weld metal, becoming trapped as it solidifies, and thus forming pores into the solid phase. Porosity can range from being extremely fine, also called microporosity, to coarse pores, order of millimeters in diameter. The culprit in case of aluminum is hydrogen. It has high solubility in molten Al but very low solubility in the solid state. When filler metal is used porosity tends to increase. This is due to the contamination of the wire. The sources of hydrogen are varied, but welding consumables are of extreme importance. The gas used in the process is a source of moisture through the water content. The ideal gas should have a dew point of less than –50°C; the welding wire should be cleaned with a lint-free cloth and a good degreasing before use. In this particular case, considering that only one sample exhibited such massive porosity, it can be assumed that a contaminant has reached the surface after cleaning.

The intimate morphology of decohesion surfaces is given in Fig. 6, for both unwelded (Fig. 6 *a*) and welded metal (Fig. 6 *b*). The unwelded base metal exhibits a fracture of mixed morphology, transcrystalline and cellular. In Fig. 6 *a*, a crack crosses the structure. Fracture separated the material on the cleavage planes in the eutectic silicon precipitates. Among the silicon particles microneck of elongated plastic solid solution can be observed.

Fig. 6 *b* reveals the surface of a welded rich pore surface. So the active surface of the metal is consistently reduced. Although the pores presence reduces the active surface, the tensile test values are frequently higher than for the unwelded material.

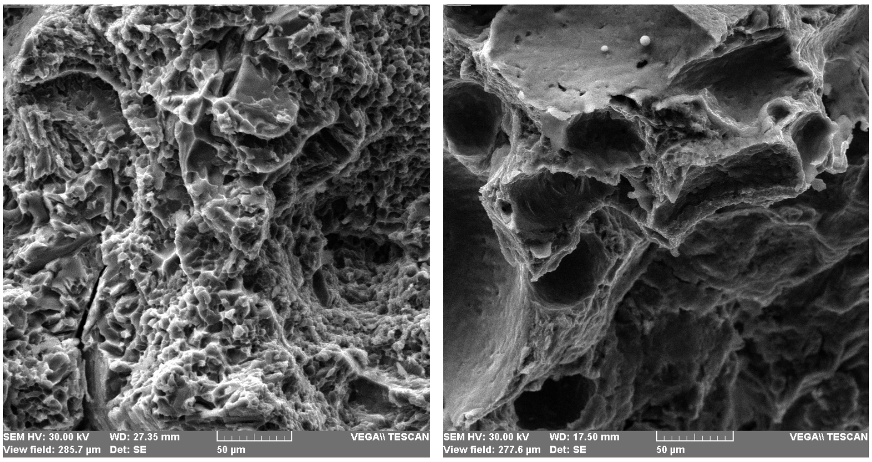

a *b*

Fig. 6 – SEM images of the fractured surfaces: *a* – unwelded metal; *b* – weld.

4. Conclusions

The AlSi11 alloy has generally good strength after welding. The fractographic study of the surfaces after tensile test proves that the most frequent discontinuity type is pore. Even if cracks are in the base material and their growth is fast, pores diminish the active surface and through this, the strength of the joint. Much more efforts must be done for pores incidence come down.

REFERENCES

Katsas S.J., Nikolaou J., Papadimitriou G., *Microstructural Changes Accompanying Repair Welding in 5xxx Aluminium Alloys and their Effect on the Mechanical Properties.* Materials and Design, *27*, 968-975 (2006).

Safta V.I., Safta V.I., *Incercările tehnologice şi de rezistență ale îmbinărilor sudate sau lipite*. Edit. Sudura, Timişoara, 2007.

STUDIUL FRACTOGRAFIC AL RUPERII IMBINARILOR WIG PE ALIAJUL AlSi11

(Rezumat)

Aluminiul şi aliajele sale joacă un rol major în economia zilelor noastre. Sudarea aliajelor de aluminiu este o practică curentă, aşa cum se întâmplă cu multe alte materiale metalice. Aliajele de aluminiu prelucrate prin deformare plastică sunt frecvent sudate, sudabilitatea lor fiind cercetată în profunzime, dar aliajele destinate prelucrării prin turnare nu au acelaşi interes. În cadrul aliajelor pentru turnare, aliajele AlSi sunt practic inexistente din punct de vedere al sudorilor. Se analizează cateva aspecte specifice privind suprafețele rezultate în urma ruperii la încercarea la tracțiune a probelor din AlSi11 sudate WIG. Se demonstrează astfel că suprafețele de rupere sunt foarte asemănătoare cu cele rezultate prin ruperea materialului de bază nesudat şi că modificările majore sunt asociate discontinuităților de la sudare.

BULETINUL INSTITUTULUI POLITEHNIC DIN IAŞI
Publicat de
Universitatea Tehnică „Gheorghe Asachi” din Iaşi
Tomul LIX (LXIII), Fasc. 1, 2013
Secţia
ŞTIINŢA ŞI INGINERIA MATERIALELOR

TEMPERATURE OF GRAPHITE NUCLEI FORMATION IN CAST IRONS, IN THERMODYNAMIC EQUILIBRIUM CONDITIONS

BY

VASILE COJOCARU FILIPIUC[*]

“Gheorghe Asachi” Technical University of Iaşi
Faculty of Material Science and Engineering

Received: February 28, 2012
Accepted for publication: March 7, 2012

Abstract: This paper explains if non-metallic inclusions with compact crystallographic lattice exists in the liquid iron, heterogeneous graphite germination occurs and eutectic graphite grows shaped as those non-metallic inclusions. If the crystallographic lattice of the non-metallic inclusions is loose, eutectic graphite is thought to grow as eutectic cells with flaky graphite, whereas primary graphite is thought to grow flake-like.

Keywords: thermodynamic activity of carbon; crystallographic lattice; non-metallic inclusions; iron.

1. Introduction

Here is an analysis of irons based on the Fe-C binary thermodynamic equilibrium diagram (Fig. 1) (Alexandru, 1979). My analysis relied on the detail with practical implications (Fig. 2) (Concise Metals Engineering Data, 1997).

Jukov (1992), traced the carbon isoactivity curves on the Fe-C thermodynamic equilibrium diagram detail, both in the solid state-specific temperature range and in the liquid state-specific temperature range (Fig. 3).

---

[*] *e-mail*: cojocaru52@yahoo.com

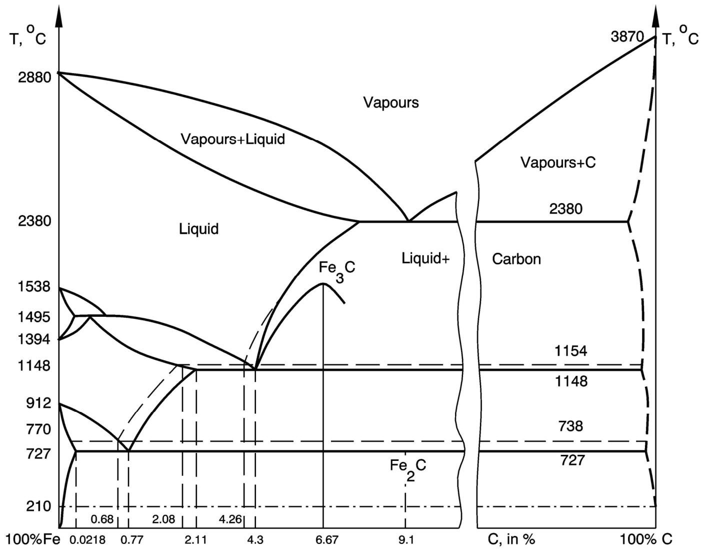

Fig.1 – Fe-C binary thermodynamic equilibrium diagram.

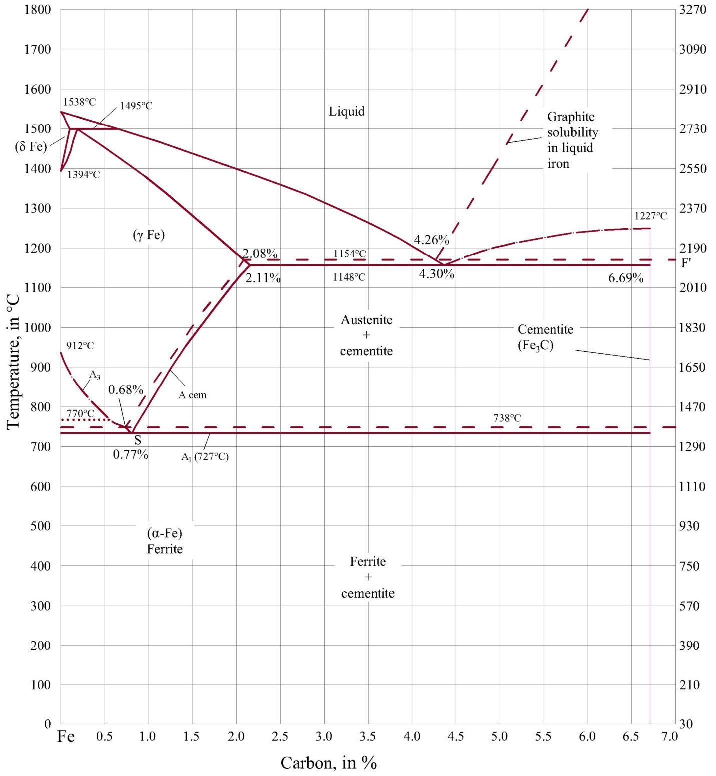

Fig. 2 – Detail of the Fe-C binary thermodynamic equilibrium diagram.

Fig. 3 shows the carbon isoactivity curves, where the value 1 of the carbon activity is found along the *P'S'K'*, *S'E'*, *E'F'* and *C'D'* curves.

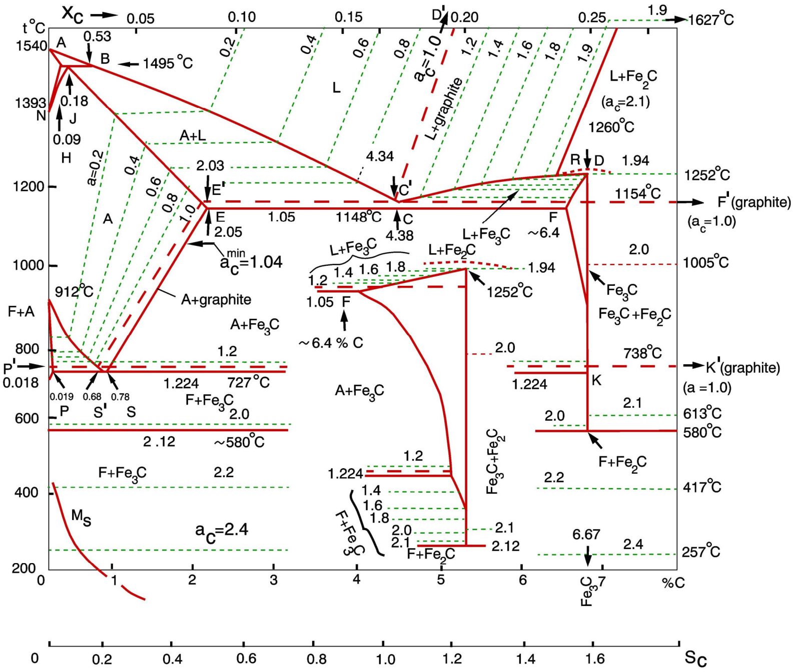

Fig. 3 – Carbon isoactivity curves on the detail of the Fe-C binary thermodynamic equilibrium diagram. S_c – degree of saturation in carbon; *A* – austenite; *F* – ferrite*;* a_C – carbon activity; *L* – liquid; X_C – carbon molar fraction; *C* – cementite.

The structural transformations occurring in the solid state, with the involvement of the liquid state (Sofroni, 1975, 1985; Laplanche, 1975), show that graphite results at the temperatures specific to the above curves, in the solid or liquid phase; eutectoid graphite is thus obtained for the *P'S'K'* curve, secondary graphite for the *S'E'* curve, eutectic graphite for the *E'F'* curve and primary graphite for the *C'D'* curve, respectively.

Graphite separation in the liquid phase, for the *E'F'* and *C'D'* curves, is representative for iron inoculation.

The first stage of graphite separation in the liquid state is the formation of graphite nuclei.

During the cooling, the graphite nuclei are formed at different temperatures, just as the iron is hypoeutectic, eutectic or hypereutectic. For hypoeutectic and eutectic irons, the graphite nuclei are formed along the *E'C'* curve, while for hypereutectic iron, the graphite nuclei are formed along the *C'D'* and *C'F'* curves, and within the solidification range, that is between the *C'D'* and *C'F'* curves.

Graphite nuclei are formed only when the carbon thermodynamic activity is 1, that is along the *E'C'*, *C'D'* and *C'F'* curves and between the *C'D'* and *C'F'* curves, which are the only cases when the carbon activity is 1.

During the cooling of the liquid phase – of the liquid metallic matrix) –, at temperatures specific to the above mentioned curves, the carbon particle clusters are stabilized and their energy conditions are suitable for the formation of the type *P* four atom cell. This is the hexagonal graphite nucleus.

The higher the fluctuation of the carbon particles, the higher the number of graphite nuclei obtained.

Carbon particle fluctuation may be enhanced by increasing the cooling rate, which determines the increasing of the degree of undercooling of iron, and, also, by a series of chemical elements of the metallic matrix, which decrease carbon solubility in liquid iron, that is they increase carbon thermodynamic activity.

This occurs when the cooling of the engineering cast iron is done in normal conditions. Such graphite germination processes are called homogeneous germination.

The cooling rate may increase the number of graphite nuclei up to a certain level, called critical threshold; if the cooling rate value exceeds this level, interdendritic graphite is formed, while very high values lead to cast iron solidification as mottled cast iron (in extreme cases, cast iron solidification occurs in the Fe-C metastable system).

The degree of undercooling is increased by various means, such as: high cast iron purity (which requires metallic bath processing), iron superheating in the liquid state, extended maintaining of the iron in a liquid state and iron manufacture in depressed atmosphere, for example.

Carbon particle fluctuation enhancing may also be achieved by other means, namely by artificially triggering a carbon diffusion process, through interventions outside the iron bath. This occurs in the metallic bath, in the metallic matrix, on chemical equilibrium incidence.

2. Graphite Nuclei Growth – Morphological Growth and Growth on Non-Metallic Inclusions

According to the equilibrium diagram, the graphite nuclei obtained undergo a radial growth at eutectic temperature, in the Fe-C binary system and in a specific temperature range, in the engineering cast irons, and they constitute the eutectic transformation (Laplanche, 1975) and form eutectic cells. In space, eutectic graphite has a small leafy appearance in the engineering cast irons. In hypereutectic cast irons, the graphite nuclei also grow within the solidification range as small leaves the geometrical shape of which depends on the chemical composition of the engineering cast iron and the size of which increases with the decrease of carbon solubility in liquid iron after the *D'C'* curve.

Since the attraction forces between the carbon atoms in a plane of graphite small leaf are very strong (covalent), graphite grows especially in the small leaf plane.

The perpendicular graphite growth on the small leaves is barely noticeable, since the attraction forces between two atoms located in different small leaves are weak (Van der Walls).

Graphite growth leads to a small plate-shaped single crystal in an engineering cast iron. The resulted small plate is not a parallelepipedic block. Its shape varies depending on the chemical composition of the cast iron. If the Fe-C stable system has suitable solidification conditions, the graphite plates should have a quasi-parallelepipedic shape in the Fe-C binary system.

The graphite nuclei in an engineering cast iron undergo a radial growth (in length, width and thickness) and make up eutectic graphite small plates, in the Fe-C binary system and in the eutectic temperature range; this growth is a complex mechanism involving a series of factors like the solid-liquid interface advance rate (eutectic liquid crystallization rate), the dissociation rate of iron and other chemical elements carbides (rate of occurrence of new graphite nuclei), the graphite nuclei growth rate, the cooling rate, the undercooling degree, etc.

If sample cross-sectioning is performed, the graphite small plates are lamella-shaped.

Fig. 4 shows the eutectic graphite small plate growth in a eutectic cell (Laplanche, 1975).

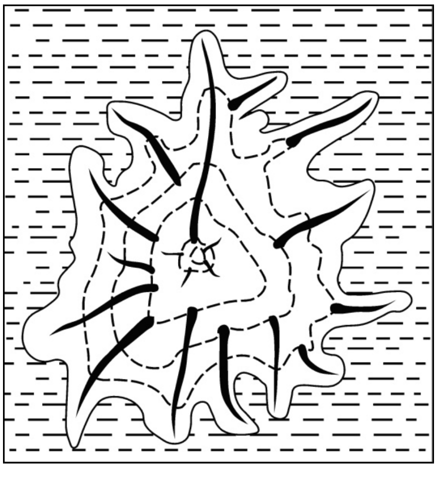

Fig. 4 − Representation of a eutectic graphite small plate growth sequence in a eutectic cell (Laplanche, 1975).

Fig. 5 shows a eutectic cell in a particular cast iron after solidification (Shiao *et al.*, 1999).

The primary graphite single crystals in hypereutectic cast irons are also small plate-shaped; they are, however, bigger than eutectic graphite single crystals.

If the cooling rate is higher than the critical threshold, the eutectic graphite small plates have an interdendritic arrangement, since eutectic austenite overlaps primary austenite.

The eutectic and primary graphite small plates have very variable shapes, which depend on the growth directions with minimum energy. Fig. 5 shows the representation of eutectic graphite small plates shaped like “hair pins”.

The graphite growth morphology described here is in perfect agreement with the Fe-C thermodynamic equilibrium diagram.

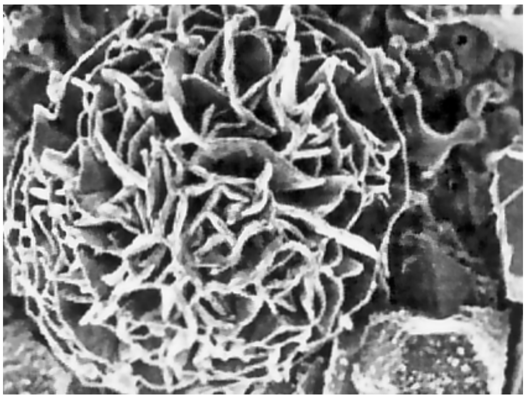

Fig. 5 – Eutectic cell in a particular cast iron (Shiao *et al.*, 1999).

Fig. 6 shows the drawing of a metallic system made up of phases 1 and 2, where phase 2 is artificially created.

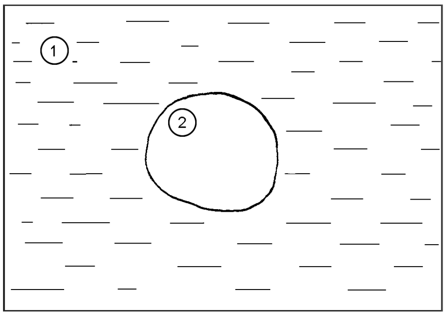

Fig. 6 – Drawing of a metallic system made up of two phases: 1 – liquid metallic matrix; 2 – new phase.

The chemical element F_j is inserted in the metallic matrix as granules.

The granules are usually macroscopic.

After milling, the granules may be nanometric. Therefore, the chemical element F_j may be used as granules, the size of which depends on the goal of the inoculation process.

Once inserted in the metallic matrix, the F_j granules make up a thermodynamic phase – *i.e*. phase 2.

As phase 2 only contains the chemical element F_j, the chemical potential of the chemical element E_2 is zero in phase 2 and it has a definite value in the metallic matrix. This results into a high activity gradient of the chemical element E_2, which triggers the diffusion of the E_2 particles from the metallic matrix towards phase 2, according to the law of the tendency to chemical equilibrium.

The F_j granules must be smaller than the biggest size allowed, which is a critical size.

If the granules are smaller than the critical size, the crystalline body of E_2 may grow around them.

Very small granules, *i.e.* those that appear as metallic powder, are obtained by different methods, such as (Cojocaru, 1997; Surdeanu & Perneş, 1984):

a) mechanical methods employed to obtain metallic powders (milling in ball mills, in lifting jacks mills, in hammer mills, in ball vibrating machines, etc.);

b) physical-mechanical methods;

c) water spraying;

d) chemical methods (oxide reduction using gaseous and solid reducing agents, etc.);

e) metallic-thermal reduction procedures;

f) physical-chemical methods (aqueous solution electrolysis, salt melt electrolysis, etc.), etc.

The metallic powder production methods according to which the shape of the metallic powders produced must be spheroidal have a practical interest. Among them, the metallic powder production technology by disk pulverization is the most frequent, where the powder particles are also subjected to the chemical reduction of the oxide film that covers the powder particles. Milling techniques using mills are also employed in industrial practice (Amza, 1997).

Fig. 7 is the drawing of a crystalline body of E_2 grown on an F_j granule. Thus, *a* is the growth of the crystalline body of E_2 around a small particle of powder of spherical F_j, *b* is the growth on a small particle of powder of elongated and angular F_j, and *c* is the growth on a big particle of powder of elongated and angular F_j.

According to Fig. 7, if the particle of powder of F_j is smaller than the critical one and it has a spherical shape, the result is a spherical crystalline body of E_2. If the particle of metallic powder is smaller than a critical one, yet its shape is angular and elongated, the crystalline body of E_2 that is produced is angular and elongated. The angular and elongated shape of the crystalline body of E_2 creates additional tension in the metallic material by strangulation the force lines. If the particle of metallic powder is bigger than the critical one and its shape is angular and elongated, the crystalline body of E_2 growing around the particle of metallic powder is either discontinuous or thin, which causes the E_2 single crystals to dissolve over a short time and, hence, the inoculation phenomenon to disappear. The same happens if the particle of powder of F_j is big and spherical.

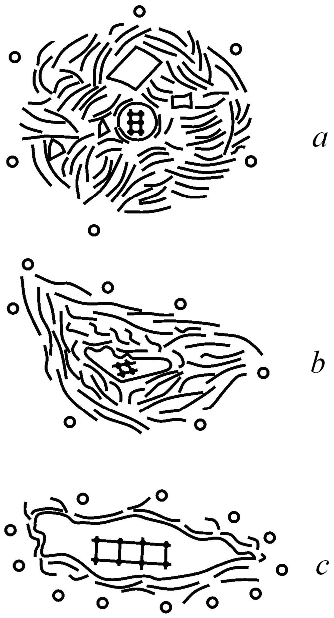

Fig. 7 – Drawing of a crystalline body of E_2 grown on an F_j granule: *a* – small spherical phase 2; *b* – small angular and elongated phase 2; *c* – big angular and elongated phase 2; ○– E_2 particles; # – phase 2; the white background around the crystalline bodies of E_2 is the metallic matrix.

The crystallographic structure of phase 2 – *i.e.* of the chemical element F_j – is extremely important. Thus, the E_2 particles penetrating the crystallographic lattice of the chemical element F_j decrease the activity gradient of the chemical element E_2 in the metallic system. The activity gradient decrease suffered by the chemical element E_2 (Δa_{E_2}) is attributed to the increase of the activity of the chemical element E_2 (a_{E_2}) in phase 2. Thus, the E_2 particles "arriving" by diffusion from the metallic matrix do not initially gather around phase 2, but they diffuse down to the middle of phase 2, due to the very high activity gradient of the chemical element E_2 (phase 2 does not contain E_2). Thus, the activity of the chemical element E_2 in phase 2 increases, whereas the activity gradient of the chemical element E_2 in the metallic system decreases. Therefore, E_2 nuclei formation around phase 2 is initially excluded. The activity gradient decrease suffered by the chemical element E_2 decreases the diffusion rate of the chemical element E_2 through the metallic matrix. Since the temperature of the metallic matrix decreases continuously, the diffusion rate decreases for the same reason. Consequently, the E_2 nuclei stop forming, or they continue as nuclei that are very easily dissolved since they lack thermodynamic stability, or they even partially grow, whereas the E_2 single crystals formed dissolve in the metallic matrix, since they lack thermodynamic stability in the alloy.

According to the analysis conducted in the previous paragraph, the E_2 particles should not penetrate the crystallographic lattice of the chemical element F_j. Therefore, the crystalline lattice should ensure a compact atom arrangement, *i.e.* the atoms should take up more space in a volume than the interstices.

The hexagonal compact atom package is characteristic of Mg, Be, Zn, Cd, Te, Ti, Zr, Hf, Sr, Os, etc.

The cubic compact package is characteristic of Cu, Au, Ag, Al, Pb, γ-Fe, Ca, Sr, Pb, Th, Nb, α-Co, Ni, Rh, etc. (Mitoşeriu & Mitoşeriu, 1998).

The package compaction concept is defined as the ratio between the volume of the particles in the unit cell and the volume of the cell in %, which is 52% in the simple cubic lattice, 68% in the cubic lattice with centered volume, 74% in the cubic lattice with centered faces and 74% in the hexagonal compact lattice.

Therefore, the most compact package occurs in cubic lattices with centered faces and in hexagonal compact lattices (package compaction goes up to 81.5% in some ionic crystals).

An octahedral interstice may shelter a foreign atom, the atomic radius of which is 0.414 of the radius of a basic atom.

A tetrahedral interstice may shelter a foreign atom, the atomic radius of which is 0.225 of the radius of a basic atom.

Consequently, compact crystallographic arrangements are cubic compact and hexagonal compact. The interstices in simple hexagonal compact arrangements take up less space than in simple cubic compact arrangements.

The crystalline bodies of E_2 dissolve faster in the metallic matrix, when no inoculating agent atoms are adsorbed on the crystalline bodies of E_2. In order to produce new materials, they have to solidify immediately after the formation of the crystalline bodies of E_2.

The chemical element F_j may be metal, metalloid or non-metal.

Whenever non-metallic inclusions with compact crystallographic lattice exist in the liquid iron, heterogeneous graphite germination occurs, and eutectic graphite grows shaped as those non-metallic inclusions (initially, there is a larger amount of carbon particles around the non-metallic inclusions). If the crystallographic lattice of the non-metallic inclusions is loose, eutectic graphite is thought to grow as eutectic cells with flaky graphite, whereas primary graphite is thought to grow flake-like.

3. Conclusions

1. The inoculating agent granules must be smaller than the biggest size allowed, which is a critical size.
2. The metallic powder production methods according to which the shape of the metallic powders produced must be spheroidal have a practical interest.
3. If the particle of powder of inoculating agent is smaller than the critical one and it has a spherical shape, the results is a spherical crystalline body of the chemical element which has a great diffusion rate through the metallic matrix.
4. The chemical element which has a great diffusion rate for particles should not penetrate the crystallographic lattice of the inoculating-agent. Therefore, the crystalline lattice should ensure a compact atom arrangement (to obtain a spheroidal for the new phase).
5. The hexagonal compact atom package is characteristic of Mg, Be, Zn, Cd, Te, Ti, Zr, Hf, Sr, Os, etc.
6. The cubic compact package is characteristic of Cu, Au, Ag, Al, Pb, γ-Fe, Ca, Pb, Th, Nb, α-Co, Ni, Rh, etc.
7. If the crystallographic lattice of the non-metallic inclusions is loose (the inoculating-agent may not have a loose crystallographic lattice) eutectic graphite is thought to grow as eutectic cells with flaky graphite, whereas primary graphite is thought to grow flake-like.

REFERENCES

Alexandru I., *Metalurgie fizică*. Institutul Politehnic, Iaşi, 1979.

Amza G., Dumitru G.M., Rândaşu V.O., *Tehnologia materialelor*. Vol. **I**, Edit. Tehnică, Bucureşti, 1997.

Cojocaru M., *Producerea şi procesarea pulberilor metalice*. Matrix Rom., Bucureşti, 1997.

Jukov A.A., F*e-C. The Stable and Metastable Equilibria*. Giessereiforschung, 1992, 106-112.

Laplanche H., *Les fontes et leurs traitements thermiques*. Pyc-Edition-Desforges, Paris, 1975.

Mitoşeriu O., Mitoşeriu L., *Cristalografia*. Vol. **I**, Edit. „Porto-Franco”, Galaţi, 1998.

Shiao F.T., Lui T.S., Chen L.H., Chen S.F., *Eutectic Cell Wall Morphology and Tensile Embrittlement in Ferritic Spheroidal Graphite Cast Iron*. Metallurgical and Materials Trans. A., **30**, *7*, 1775-1784 (1999).

Sofroni L., *Elaborarea şi turnarea aliajelor. Fonte. Oţeluri. Aliaje neferoase*. Edit.

Didactică şi Pedagogică, Bucureşti, 1975.

Sofroni L., Ripoşan I., Brabie V., Chişamera M., *Turnarea fontei.* Edit. Didactică şi Pedagogică, Bucureşti, 1985.

Surdeanu T., Perneş M., *Piese sinterizate din pulberi metalice*. Edit. Tehnică, Bucureşti, 1984.

* * * *Concise Metals Engineering Data.* A.S.M. Internat., Davis R.V. (Ed.), 1997.

TEMPERATURA DE FORMARE A NUCLEILOR DE GRAFIT IN FONTA TURNATĂ, ÎN CONDIȚII DE ECHILIBRU TERMODINAMIC

(Rezumat)

Se explică faptul că, dacă în fonta lichidă se află incluziuni nemetalice cu rețeaua cristalografică compactă, are loc germinarea eterogenă iar grafitul eutectic creşte sub forma respectivelor incluziuni nemetalice. Dacă incluziunile nemetalice au rețeaua cristalografică necompactă, se apreciază că grafitul eutectic creşte sub formă de celule eutectice cu grafit lamelar iar grafitul primar sub formă de lamelă.

BULETINUL INSTITUTULUI POLITEHNIC DIN IAŞI
Publicat de
Universitatea Tehnică „Gheorghe Asachi” din Iaşi
Tomul LIX (LXIII), Fasc. 1, 2013
Secţia
ŞTIINŢA ŞI INGINERIA MATERIALELOR

PRODUCTION OF CORAL-LIKE GRAPHITE CAST IRON

BY

VASILE COJOCARU FILIPIUC[*]

“Gheorghe Asachi” Technical University of Iaşi
Faculty of Material Science and Engineering

Received: February 28, 2012
Accepted for publication: March 7, 2012

Abstract: The mechanism of coral-like graphite formation is identical to the mechanism of compacted graphite formation. Coral-like graphite is produced only when the interfacial surface tension between the metallic matrix and the inoculating agent drops is low (than a critical value). The presence of surface-active elements in the inoculating agent drops is essential, as they determine the low value of the interfacial surface tension. The surface-active elements should be adsorbed on graphite, so that the coral-like graphite value would not dissolve in the metallic matrix in a short time.

Keywords: coral-like graphite; interfacial surface tension; zirconium; adsorption.

1. Introduction

The mechanism of coral-like graphite formation is identical to the mechanism in Fig. 1.

Coral-like graphite cast iron is a particular case of compacted graphite cast iron.

Fig. 2 shows various types of coral graphite (Lux, 1975).

The main factor influencing coral-like graphite production is the interfacial surface tension between the metallic matrix and the inoculating agent drops.

---

[*] *e-mail*: cojocaru52@yahoo.com

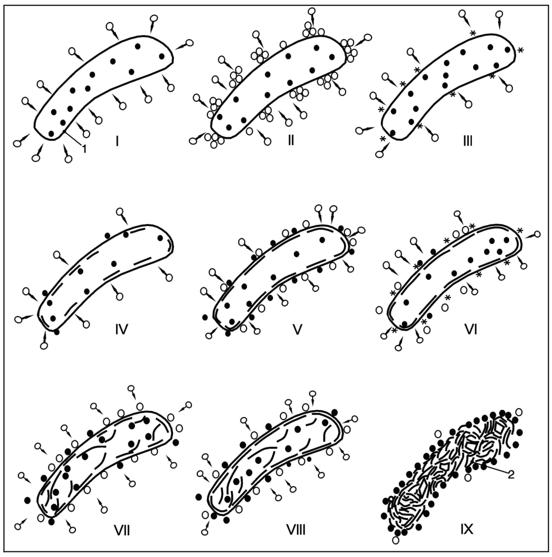

Fig. 1 – Drawing of the mechanism of compacted graphite formation in the inoculating agent drops: • – inoculating agent atoms and surface-active elements; ∘ – carbon particles; (,▭ – graphite single crystals; 1 – inoculating agent drops; 2 – crystalline body of compacted graphite; * – graphite nuclei; the white background around the drops is the metallic matrix.

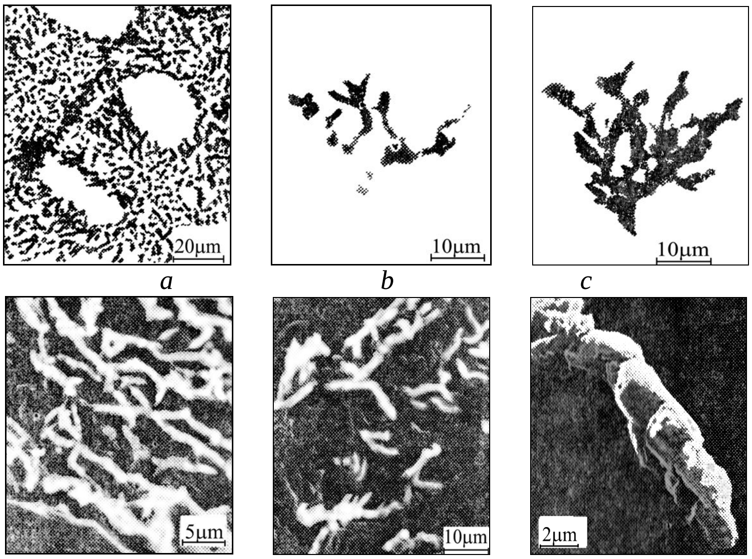

a *b* *c*

d *e* *f*

Fig. 2 – Various types of coral-like graphite. *a*, *b*, *c* – microstructures analyzed using an optic microscope; *d*, *e* and *f* – microstructures analyzed using a scanning microscope (Ripoşan & Sofroni, 1984).

Fig. 3 shows the drawing of a metallic system made up of phases 1 and 2, where phase 2 is artificially created.

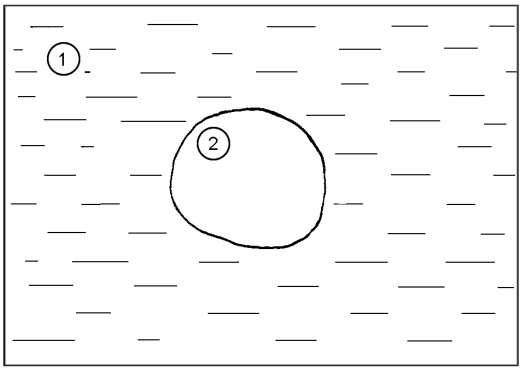

Fig. 3 – Drawing of a metallic system made up of two phases. 1 – liquid metallic matrix; 2 – new phase.

Coral-like graphite is the compacted graphite with the largest surface. The graphite shown in Fig. 4 may be considered the standard coral-like graphite and it may be characterized as multiple bifurcate graphite.

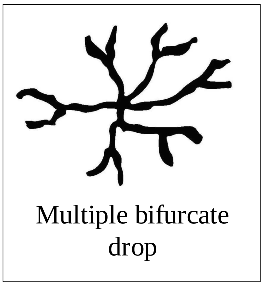

Fig. 4 – Multiple bifurcate shape of phase 2, when the σ_{12} interfacial surface tension is very low (Andelman & Rosensweig, 2009).

Coral-like graphite is produced only when the interfacial surface tension between the metallic matrix and the inoculating agent drops, σ_{12}, is low, more precisely lower than a critical threshold. When σ_{12} is higher than a critical threshold, the graphite produced is compacted.

Coral-like graphite is produced by iron inoculation using inoculating agents found in the liquid state at the iron inoculation temperature.

According to Fig. 1, the carbon particles diffuse from the metallic matrix towards the drops due to the high carbon activity gradient between the metallic matrix and the inoculating agent drops – 1st sequence.

The inoculating agents with densities lower than that of the liquid metallic matrix, at the inoculation temperature, are the most common in industrial practice. Therefore, the graphite nuclei will grow in drops.

Carbon particles diffuse continuously and hence carbon particle agglomerations occur at the metallic matrix-inoculating agent drop interface (2nd sequence).

The sequences marked I, II and III show the maximum contact surface between the metallic matrix and the drops, which is the very surface of the drops.

A higher carbon particle concentration around the drops means a higher molar fraction of carbon and, hence, a higher carbon activity.

The chemical composition of the metallic matrix must ensure the highest possible carbon activity, which should be as close to 1 as possible. For instance, this is achieved in practice for little hypoeutectic, eutectic and hypereutectic irons.

Carbon activity reaches 1 due to the carbon concentration increase and the carbon activity coefficient increase caused by the decrease of the temperature of the metallic matrix. Hence, hexagonal graphite nuclei are formed in the interface area, 3rd sequence, where the graphite nuclei are marked by asterisks.

The graphite nuclei start to grow in drops, since the carbon particles diffuse continuously.

The contact surface between the metallic matrix and the drops (4th sequence) decreases with the increase of the graphite single crystals, and it becomes minimal when the junction between the graphite single crystals is done, 5th sequence.

A graphite single crystal is a phase, which means that there no longer is a direct contact between the metallic matrix and the drops around it, and therefore there is no carbon activity gradient between the two phases (metallic matrix and drops). Hence, the carbon particles stop diffusing. On the other hand, there is a direct contact between the metallic matrix and the drops where the junctions between the graphite single crystals occur, and where the process of carbon particle diffusion continues and generates new graphite nuclei - 6th sequence.

When the graphite single crystals grow, the inoculating agent particles and the surface-active element particles diffuse outside the drops, in the interface area.

The surface-active element particles have the specific capacity of gathering in the interface area; however, at the same time, some surface-active elements also have different capacities of dissolving in the metallic matrix. Fig. 5, for instance, shows that chemical elements such as Ni, Cu, Si, V, etc. also dissolve in the metallic matrix, although they are surface-active elements. Hence, one may conclude that the surface-active elements included in the chemical composition of the inoculating agents should not dissolve in the metallic matrix, that is in Fe. Yet, if the dissolution does occur, the saturation point should be very low. This requirement is accounted for by the need of the surface-active elements to remain in the metallic matrix-drop interface, so that, in the end, after the completion of the crystalline bodies of graphite, the surface-active elements in the interface and the inoculating agent particles would be adsorbed on the crystalline bodies of graphite, thus significantly delaying their dissolution in the metallic matrix.

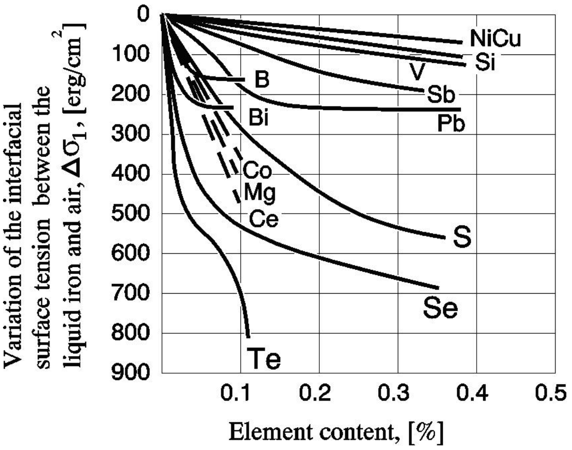

Fig. 5 – Influence of certain surface-active chemical elements in the iron on the interfacial surface tension between the liquid iron and air, for a specific iron (Sofroni *et al.*, 1978).

For both compacted graphite and graphite nodule formation, emphasis is laid on the major role played by the silicon in the inoculating agent that diffuses in the metallic matrix, around the inoculating agent drops, in order to enhance carbon activity. The important role played by the iron in the inoculating agent is also underlined, as it increases the drop density and it does not diffuse in the metallic matrix due to the negative activity gradient (the iron activity in the metallic matrix is higher than the iron activity in the inoculating agent drops).

The new graphite nuclei formed in the interstices between the graphite single crystals in the first single crystal layer start to grow in the inoculating agent drops, which determines the mechanical impact between the growing graphite single crystals and the graphite single crystals in the first layer. That mechanical impact materializes in the dislocation of graphite single crystals found in the first layer and their directing towards the middle of the drops. The inoculating agent particles diffuse towards the outside of the drops during graphite single crystal dislocation, while the contact surface between the metallic matrix and the inoculating agent drops increases, 7th sequence. The carbon particle diffusion flow from the metallic matrix towards the inoculating agent drops is thus increased, and the growth of the graphite single crystals found in the second layer is also enhanced. This is followed by the junction between the graphite single crystals, 7th sequence. The formation of new graphite nuclei and their growth as single crystals are repeated until the inoculating agent drops are "filled" with graphite single crystals, 9th sequence. The 9th sequence shows that all the inoculating agent particles (the inoculating chemical elements and the surface-active chemical elements) are in the metallic matrix-compacted graphite interface.

Multiple bifurcate graphite, shown in Fig. 4, has thin branches, due to which the time of dissolution in the metallic matrix is very short.

The basic specificity of coral-like graphite consists of the presence of the inoculating element or elements, as well as of the surface-active element or elements, throughout the coral-like graphite surface.

The presence of surface-active elements in the inoculating agent drops is essential, as they determine the low value of the σ_{12} interfacial surface tension.

The surface-active elements should be adsorbed on graphite, so that the coral-like graphite would not dissolve in the metallic matrix in a short time.

In addition to the remarks included in the two previous paragraphs, what is equally important is that the surface-active element or elements should not be very chemically reactive, that is they should not chemically interact with the elements in the metallic matrix, as this would trigger a phenomenon of desorption of the surface-active element or elements and the coral-like graphite would dissolve very quickly.

The period of formation of the crystalline bodies of coral-like graphite is very short, as the coral-like graphite branches are thin. Since the carbon activity gradient is very high when the coral-like graphite inclusions are completed, much higher than the carbon activity gradient at the time of inoculating drop formation, the carbon diffusion rate is very high, the dissolution rate of the crystalline bodies of graphite is also very high, unless there are particles adsorbed on the graphite surface.

The second important requirement to be met is that the cooling of the coral-like graphite cast iron should occur at high rate, so that the coral-like graphite would be caught in the solidification front, *i.e.* the dissolution process would be stopped.

If the inoculating agent drops originally looked like in figure 4 and the crystalline bodies were coral-like graphite, multiple bifurcate graphite, despite the high cooling rate, whole branches of multiple bifurcate graphite would have been dissolved in the metallic matrix and the coral-like graphite would have looked like in Fig. 2 *a*, due to large amounts of surface-active elements that dissolve relatively easily in the hot metallic matrix. Such graphite is also called chunky graphite and is found especially in the thermal axis of thick walls, in nodular graphite cast iron. This phenomenon occurs in most surface-active elements, with the exception of zirconium (we refer mainly to the surface-active elements present in the inoculating agent, without however leaving aside those found in the irons). Coral-like graphite and chunky poorly branched or even unbranched graphite have D sizes, ASTM, and reference (Ripoşan & Sofroni, 1984) considers them to be type I graphite.

According to Apostolescu (1982), zirconium in the inoculating agent (Campomanes & Goller, 1975) is considered a poorly nodulizing surface-active element and, hence, a surface-active element with low chemical reactivity and high graphite adsorption forces. Therefore, when inserted in the inoculating agent, zirconium will be adsorbed on graphite when the crystalline bodies of graphite are done growing.

The zirconium adsorbed on the coral-like graphite determines the stability of the coral-like graphite and its production as such. In such case, coral-like graphite cast iron castings may also be manufactured at low cooling rates, both thick wall castings and castings manufactured by pouring in moulding sand moulds.

Coral-like graphite is also similar to the graphite in the eutectic cells and the resemblance consists of the branches of the graphite small leaves. For instance, if the cooling rate of an unalloyed hypoeutectic cast iron is high during the eutectic transformation, some of the branches of the eutectic graphite skeleton in a eutectic cell disappear and the eutectic graphite acquires a coral-like graphite shape. A high cooling speed during the eutectic transformation is achieved, for instance, by pouring the iron in metallic or graphite moulds. In regular industrial unalloyed cast irons, the sulphur content is high, as it even exceeds 0.1%. During the growth of the graphite lamellae (small leaves), the sulphur, which is a powerful surface-active element for iron, is separated in the interface area, that is at the metallic matrix-graphite interface as well. From this standpoint, the sulphur in the cast iron is a surface-active element that significantly decreases the σ_{12} interfacial surface tension. At the same time, however, sulphur increases the carbon activity coefficient a lot. Sulphur also decreases carbon solubility in liquid iron even more than silicon, aluminum and phosphorus. At 1,600^{o}C for instance, 1% of sulphur decreases carbon solubility in liquid iron by 0.4%, 1% of silicon decreases it by 0.3%, 1% of aluminum by 0.25% and 1% of phosphorus by 0.35% (Cojocaru-Filipiuc, 2007). Therefore, sulphur enhances carbon activity considerably, which means that a higher amount of sulphur (of about 0.1%) is even recommended for flaky graphite cast iron, in order to prevent free cementite separation in the thin walls of the castings, and also to produce fine flaky graphite due to the occurrence of additional graphite nuclei at eutectic transformation, for instance, in a hypoeutectic cast iron. If the amount of sulphur in the cast iron is very small, *i.e.* of up to 0.002%, the cast iron lacks even micro-volumes where additional graphite nuclei may occur, as the graphite must undergo a morphological growth, interconnected in the eutectic cells. The role of sulphur of preventing free cementite separation in the thin walls is taken over by the 2.25% to 4% silicon that has to be present in the cast iron. The interconnectivity of the graphite small leaves decreases significantly in the eutectic cells if the cooling rate during the eutectic transformation is high, i.e. if the iron is poured in metallic moulds or in graphite moulds. Coral-like graphite is produced in the latter case. When the cooling rates during the eutectic transformation are very high, eutectic austenite merges with primary austenite, producing interdendritic-like graphite, chunky graphite or even punctiform graphite, in the presence of enhancing chemical compositions (cast irons that contain chemical elements that enhance considerably the undercooling degree of cast iron at eutectic temperature).

The presence of branches in coral-like graphite turns a coral-like graphite cast iron into a cast iron with specific features, as it enjoys shorter diffusion distances and it is processed by special thermal treatments (austempering), with the involvement of the metallographic constituent called ausferrite. In practice, the processing of coral-like graphite cast iron refers only to coral-like graphite cast iron produced by inoculation and not to that produced by the increase of the cooling rate and that containing very little sulphur.

In principle, at the end of the eutectic transformation, coral-like graphite has primary and eutectic austenite halos, respectively.

2. Conclusions

1. The mechanism of coral-like graphite formation is identical to mechanism of compacted graphite formation;

2. Coral-like graphite is produced only when the interfacial surface tension between the metallic matrix and the inoculating agent drops, σ_{12}, is low – lower than a critical threshold

3. The zirconium adsorbed on the coral-like graphite determines the stability of the coral-like graphite and its production as such;

4. In principle, at the end of the eutectic transformation coral-like graphite has primary and eutectic austenite halos, respectively.

REFERENCES

Andelman D., Rosensweig R.E., *Modulated Phases: Review and Recent Results.* J. Phys. Chem. B, **113**, *12*, 3785-3798 (2009).

Apostolescu R., *Cristalografie. Mineralogie.* Edit. Didactică şi Pedagogică, Bucureşti, 1982.

Campomanes E., Goller R., *Production of Cast Iron Containing Intermediate Forms of Graphite.* AFS Trans., **83**,1975, 55-62.

Cojocaru-Filipiuc V., N*odulizarea grafitului în fonte − aspecte teoretice*. Edit. „Politehnium”, Iaşi, 2007.

Lux B., *Discussion, Transition from undercooled to flake graphite. The Metallurgy of Cast Iron*. Georgi Publ. Co., St. Saphorin, Switzerland, 1975, 289-293; Discussion, 528.

Ripoşan I., Sofroni L., *Fonta cu grafit vermicular*. Edit. Tehnică, Bucureşti, 1984.

Sofroni L., Ştefănescu D.M., Vincenz C., *Fonta cu grafit nodular*. Edit. Tehnică, Bucureşti, 1978.

PRODUCEREA DE FONTĂ CU GRAFIT CORAL

(Rezumat)

Modificatorii trebuie să conţină elemente chimice grafitizante în cantitate mare, cum ar fi, de exemplu, siliciu. Producerea fontei cu grafit lamelar prin modificare, înseamnă modificarea fontei, adică schimbarea condiţiilor de cristalizare primară prin introducerea de modificator în fonta lichidă. Tensiunea interfazică dintre matricea metalică şi picăturile de modificator are valori mai mari în cazul geometriei de lamelă a picăturilor decât în cazul geometriilor compactizată şi coral.

BULETINUL INSTITUTULUI POLITEHNIC DIN IAŞI
Publicat de
Universitatea Tehnică „Gheorghe Asachi” din Iaşi
Tomul LIX (LXIII), Fasc. 1, 2013
Secţia
ŞTIINŢA ŞI INGINERIA MATERIALELOR

HYPOTHESE ON THE MECHANISM OF NODULAR GRAPHITE FORMATION IN MAGNESIUM

BY

VASILE COJOCARU FILIPIUC[*]

“Gheorghe Asachi” Technical University of Iaşi
Faculty of Material Science and Engineering

Received: February 28, 2012
Accepted for publication: March 7, 2012

Abstract: It is about of iron inoculation using as inoculating agent magnesium. Once the magnesium bubbles formed in the liquid iron, the carbon particles diffusion process from the metallic matrix towards the magnesium bubbles starts. The carbon atom agglomeration from metallic matrix – Mg bubbles zone, from hexagonal graphite nuclei. These nuclei begin to grow in Mg bubble and so, graphite single crystals take shape. The crystalline body of graphite produced has the same volume as the former magnesium bubble and it is called graphite nodule – nodular graphite, globular graphite or spheroidal graphite.

Keywords: nodular graphite; carbon diffusion; single crystal; graphite nuclei; bubbles.

1. Introduction

The mechanism of nodular graphite formation is shown in Fig. 1.

According to the same figure, magnesium was used as inoculating agent.

Once the magnesium bubbles formed in the liquid iron, the carbon particle diffusion process from the metallic matrix towards the magnesium bubbles starts, 1st sequence in Fig. 1.

---

[*] *e-mail*: cojocaru52@yahoo.com

According to Baum (1982), the iron particles in the liquid iron matrix may appear as both atoms and cations (C^{4+}), the latter being more numerous.

Since the carbon particles do not diffuse in the magnesium bubbles, this creates carbon particle agglomerations in the metallic matrix, in the immediate vicinity of the magnesium bubbles.

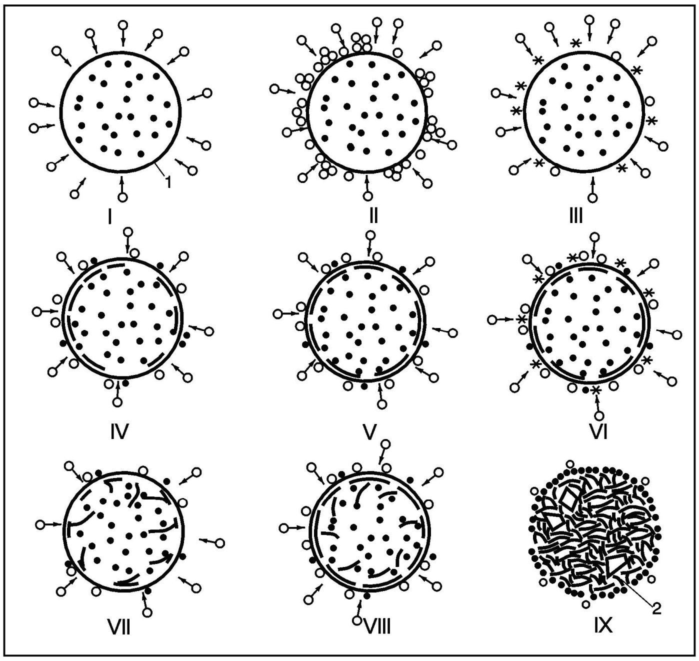

Fig.1. – Schematic representation of the mechanism of nodular graphite formation in magnesium bubbles: ● – Mg atoms; ○ – C particles; ⌒ ,□ – graphite single crystals; 1 – Mg bubble; 2 – graphite nodule; the white background around the bubbles and the graphite nodules – liquid metallic matrix; * – graphite nuclei.

If the carbon particles are C^{4+} cations, when they reach the metallic matrix-bubble interface they come in direct contact with the magnesium atoms in the bubbles.

The magnesium atoms move chaotically in the bubbles.

The higher the temperature of the liquid iron, the more chaotic the motion of the Mg atoms in the bubbles, which also means higher kinetic energy.

Due to the direct contact between the C^{4+} cations and the Mg atoms, the C^{4+} cations receive electrons from the Mg atoms and, thus, they turn into carbon atoms.

The liquid iron structure is micro-heterogeneous, as the carbon particle diffusion through the metallic matrix is uneven. Carbon atom agglomerations are thus formed at the metallic matrix-bubble interface, and they are unevenly located on the surface of the bubbles, 2nd sequence of Fig. 1.

Since the carbon particles never cease to diffuse from the metallic matrix towards the magnesium bubbles, the graphite nuclei begin to grow and graphite single crystals take shape.

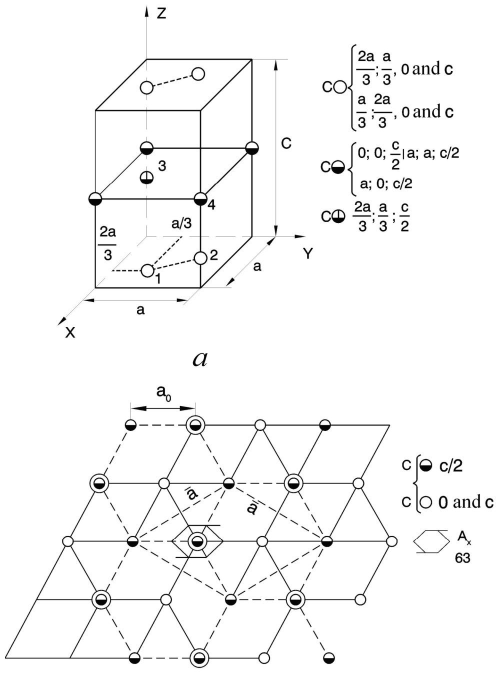

a

b

Fig.2. – Structure of hexagonal graphite: *a* – perspective projection; *b* – projection with dimension figure (Apostolescu, 1982).

The graphite nuclei also grow due to the carbon particles that move chaotically in throughout the highly pure and hot metallic matrix. In the presence of silicon and in the absence of sulphur, the chaotic motion of the carbon particles is very intense. Thus, the carbon particles are originally attracted by the carbon particles in the graphite nuclei and then by those in the graphite single crystals. Therefore, graphite nuclei and graphite single crystals also grow under the influence of other factors than the tendency towards chemical equilibrium of the carbon particles. This remark also applies to all phase 2 shapes.

Graphite nuclei start to grow in the space where the growth energy is minimum, that is they start to grow in the magnesium bubbles.

The pattern repeated in the hexagonal graphite lattice, in each lattice knot, is identical with the group of atoms marked 1, 2, 3, and 4 in Fig. 2 *a*.

Thus, graphite single crystals start to grow on the surface of the magnesium bubbles, and they are formed, at first, of two carbon atom layers located in the corners of hypothetical hexagons.

Graphite single crystal growth occurs mainly in the plane of the two basic layers, which follows the configuration of the bubble surface.

The carbon atoms that are available due to the continuous carbon particle diffusion are attracted by strong forces, of the covalent type, by the atoms in the two initial layers; these layers are marked by the pattern repeated in each lattice knot (one layer by the carbon atoms marked 1 and 2 and one layer by the carbon atoms marked 3 and 4, in Fig. 2 *a*). This explains why the first two carbon atom layers grow on the surface of the bubbles, as in the 4th sequence of Fig. 1.

Carbon particles “arrive” continuously by diffusion, in the interface area, from all directions (more carbon particles “arrive” by diffusion from certain directions, due to the lack of chemical homogeneity; in engineering cast irons, the lack of chemical homogeneity if even greater). The sequences in Fig. 1 suggest that the carbon particles follow a trajectory that is perpendicular on the surface of the bubbles. In reality, since the Mg bubbles are, for the most part, in a continuous ascending motion, the incidence angle between the carbon particles and the bubble surface is smaller than 90°.

The carbon particles “arriving” by diffusion from the metallic matrix are distributed as follows:

a) the carbon particles “arriving” at the border of the first two layers of carbon atoms (position 2 in Fig. 3) are attracted by the carbon atoms from the layers of carbon atoms, by their strong covalent bonds, and, thus, the graphite single crystal grows along the contour of the Mg bubble surface;

b) the carbon particles “arriving” in the interface area, towards the inside of the first two layers of carbon atoms, and not at their border, initiate the formation of a new layer of carbon atoms (position 3 in Fig. 3); the bond between two layers of carbon atoms is weak, of the Van der Walls type. The new layer of carbon atoms starts to grow together with the first two layers of carbon atoms, due to the carbon particles “arriving” at the border of the new layer of carbon atoms.

Fig. 3 is a detailed representation of the sequences in Fig. 1 marked IV, V, VI, VII and VIII.

In Fig. 1, the graphite single crystals are schematically represented by arcs, while in Fig. 3, the graphite single crystals are represented by shape 1.

The layers of carbon atoms are represented by arcs in Fig. 3.

After its initiation (position 3 in Fig. 3), the third new layer of carbon atoms begins its morphological growth, due to the carbon atoms “arriving” by diffusion from the metallic matrix, towards the boundary of the third layer, due to the strong covalent attraction forces between the carbon atoms.

The first two layers (position 2 in Fig. 3) grow continuously during the growth of the third layer, 2nd sequence in Fig. 3.

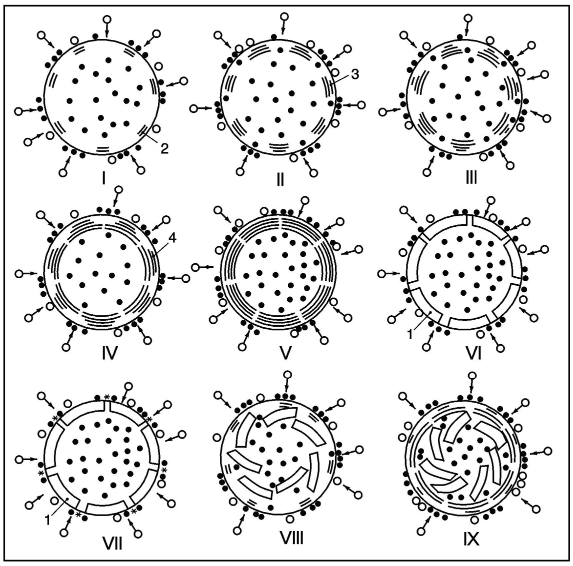

Fig. 3 – Detailed representation of the stages marked IV, V, VI, VII and VIII in Fig. 1:(– layers of carbon atoms; 1 – graphite single crystal; ● – Mg atoms; ○ – C particles; 2 – the first two layers of C atoms; 3 – the third layer of C atoms; 4 – the nth layer of C atoms. The white background around the Mg bubbles – liquid metallic matrix; * – graphite nuclei.

During the growth of the first three layers of carbon atoms, the carbon atoms “arriving” from the metallic matrix towards the middle of the third layer of carbon atoms initiate the fourth layer of carbon atoms that starts to grow just as the third layer. Several carbon atom layers are formed in this way, but their number is limited by the moment when the first two layers of carbon atoms meet the first two layers of carbon atoms of other neighboring single crystals. The last layer of carbon atoms that is formed is marked “n” and it is assigned the code 4 in Fig. 3.

After the first two layers of carbon atoms have joined the first two layers of carbon atoms of the neighboring graphite single crystals, the 4th sequence in Fig. 3, the third, fourth and nth layers continue to grow until the junctions between these layers of carbon atoms and those of the neighboring single crystals are done, in the following order: first the third, then the fourth and finally the nth layer. The 5th sequence in Fig. 3 and the 5th sequence in Fig. 1 show the moment when the junctions for all the layers have been completed. The first layer of graphite single crystals is marked 1 in the 6th sequence in Fig. 3.

Fig. 4 shows the drawing of a metallic system made up of phases 1 and 2, where phase 2 is artificially created.

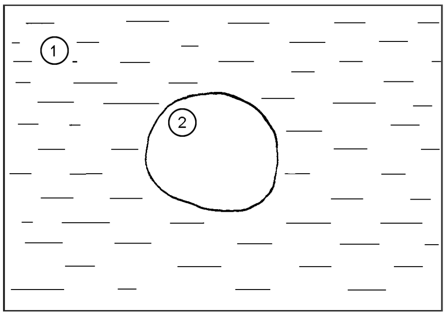

Fig. 4 – Drawing of a metallic system made up of two phases: 1 – liquid metallic matrix; 2 – new phase.

The bond between the metallic matrix (phase 1) and the magnesium bubble (phase 2) is preserved thanks to the interstices between the graphite single crystals in the first layer of graphite single crystals.

Once arrived at the metallic matrix-magnesium bubble interface, the carbon particles produce agglomerations in the interface area. Graphite nuclei occur when the carbon activity in the carbon particle agglomerations reaches 1 – 6th sequence in Fig. 1 and 7th sequence in Fig. 3.

Once formed, the graphite nuclei start to grow.

The graphite nuclei growth towards the inside of the Mg bubbles dislocates the graphite single crystals in the first row of graphite single crystals, as shown in the 8th sequence (Fig. 3) and in the 7th sequence (Fig. 1). Thus, new bonding channels between the metallic matrix and Mg bubbles are opened, which enhances the process of carbon particle diffusion through the metallic matrix, towards the magnesium bubbles.

The formation of a new layer of carbon atoms is no longer thought possible after the junction of all the carbon atom layers (2, 3 and 4 in Fig. 3), the 5th and 6th sequences in figure 3 and the 5th sequence in Fig. 1, because of the weak bonding forces between two carbon atoms located in different carbon layers and because of the configuration of the boundaries between the single crystals (the 5th and 6th sequences in Fig. 3). Only the strong graphite nuclei growth force (covalent forces) and the location of the graphite nuclei between the graphite single crystals manage to dislocate graphite single crystals from the first layer of graphite single crystals and to randomly push them towards the inside of the magnesium bubbles, the 7th and 9th sequences in Fig. 3 and the 7th and 8th sequences of Fig. 1.

Along with the graphite nuclei growth in the Mg bubble, that is along with the growth of the new graphite single crystals in the Mg particles, by reason of the tendency to mechanical equilibrium between the metallic matrix and the Mg bubbles, the Mg particles diffuse towards the outside of the Mg bubbles, in their immediate vicinity, since magnesium is not dissolved in the metallic matrix (in the liquid iron). The Mg particles diffuse through the bubble, towards the metallic matrix, that is through the wide interstices created by graphite single crystal dislocation.

The phenomena described above are repeated until the entire magnesium bubble is "filled" with graphite single crystals and all the Mg particles have diffused around the former Mg bubble, around the graphite nodule.

For instance, the crystalline body of graphite produced has the same volume as the former magnesium bubble, and it is called graphite nodule– nodular graphite, globular graphite or spheroidal graphite, the 9th sequence in Fig. 1.

The 9th sequence in Fig. 1 shows single crystals represented by circular arcs, which follow more or less the curvature of the Mg bubble surface and which, as they are pushed towards the inside of the bubbles, are oriented randomly. The schematic representation shows cross and longitudinal sections of graphite single crystals.

If the inoculating agent includes more than one chemical element, these are, for instance, a basic element with a boiling temperature lower than that of the liquid iron and one or several chemical elements, in small quantities, that are designed to decrease the content of the antiinoculant chemical elements in the liquid iron, which, as stated at the beginning of this paragraph, were identified as surface-active elements. The content is decreased to concentrations that stop being a threat to the inoculation. If, after the chemical interaction, the bubbles still contain chemical elements that accompany the basic element, they will diffuse through the graphite single crystals towards the outside of the bubbles, just as the magnesium particles shown in Figs. 1 and 3. Depending on the circumstances, the accompanying elements in the bubbles, which are dissolved in the metallic matrix (liquid iron), will be distributed, by diffusion, in the metallic matrix. The elements that fail to dissolve in the metallic matrix will be distributed around the graphite nodules (where they remain in a state of adsorption on the graphite nuclei or they are located around the metallic matrix-graphite nodules interface). Whatever the case, when the bubbles are "filled" with graphite single crystals, all the chemical elements in the inoculating agent in the gaseous state have "left" the bubbles, by diffusion, according to the law of the tendency to mechanical equilibrium, which is part of the overall thermodynamic equilibrium, together with the thermal and chemical equilibriums.

Graphite nodule completion actually marks the beginning of phase 3, as phase 2 turns into phase 3; the metallic system is still biphasic, except that it includes the metallic matrix and graphite nodule phases, phases 1 and 3. Therefore, the new biphasic equilibrium needs to be achieved, this time between the metallic matrix and the graphite nodule.

As concerns carbon, the diminution of the quantity of carbon in the metallic matrix is accompanied by the considerable decrease of the carbon activity in the metallic matrix. The fact that the carbon activity in the graphite nodules reached one supports the assumption of a high carbon activity gradient between the metallic matrix and the graphite nodules, meaning that the graphite nodules and the metallic matrix are not in a state of chemical equilibrium. This urges graphite to dissolve in the metallic matrix when the graphite nodules have completed their formation. Graphite nodule completion also coincides with the ceasing of carbon particle diffusion from the metallic matrix.

If nodular graphite formation lasts a short time (according to Loper & Heine (1961) and Loper & Heine (1963), in a specific iron, the graphite nodules are formed during the cooling of the iron from 1,350^{o}C to 1,320^{o}C), graphite nodule dissolution lasts longer, due to the inoculating agent atoms that are strongly adsorbed on the graphite nodules, for instance.

Graphite nodule dissolution starts when graphite single crystals get detached from the graphite nodules because of the weak bonding forces between two single crystals, as already discussed, the graphite single crystals get separated from the graphite nodule by ultrasound vibration. Layers of graphite atoms are said to get subsequently detached from the graphite single crystals and finally the carbon atoms in the detached layer of carbon atoms are dissolved.

Graphite nodule dissolution does not occur evenly on their surface. Since the graphite single crystals have almost the same curvature, single crystals tend to position themselves according to their radius of curvature, during graphite nodule growth, and thus to make up packs of graphite single crystals – blocks of graphite single crystals, that either get separated by blocks from the graphite nodule or remain in the graphite nodule toward the end of graphite nodule dissolution in the liquid metallic matrix. Such blocks of graphite single crystals that remain in the graphite nodules toward the end of the dissolution process currently occur in the thermal axis of the thick casting walls and they were called chunky graphite.

Graphite nodule dissolution becomes obvious if the inoculated iron is maintained in the liquid state for a longer time before being poured in the moulds.

The presence of the magnesium atoms at the metallic matrix-graphite nodule interface is very important, as it prevents the dissolution of the graphite nodules immediately after their formation. Although the chemical equilibrium law acts starting with graphite nodule completion, it is stopped or delayed by the magnesium atoms found around the graphite nodules, in the example shown in Figs. 1 and 2. It is therefore very important for the inoculating chemical elements not to dissolve in the metallic matrix, and the adsorption forces on the nodular graphite to be powerful.

2. Conclusions

1. The carbon particles diffuse towards the magnesium bubbles thanks to the chemical equilibrium tendency;
2. The carbon atom agglomerations from the Mg bubble vicinity form hexagonal graphite nuclei;
3. Graphite nuclei start to grow in the space where the growth energy is minimum, that is they start to grow in the magnesium bubbles;
4. The single crystals are represented in this paper by circular areas which follow more or less the curvature of the Mg bubbles surface;
5. If nodular graphite formation lasts a short time, graphite nodule dissolution lasts longer, due to the inoculating agent atoms that are strongly adsorbed on the graphite nodules, for instance;
6. It is very important for the inoculating chemical elements not to dissolve in the metallic matrix and the adsorption forces on the nodular graphite to be powerful.

REFERENCES

Apostolescu R., *Cristalografie. Mineralogie.* Edit. Didactică şi Pedagogică, Bucureşti, 1982.

Baum B.A., *Topituri metalice. Probleme şi sinteze*. Edit. Nauka, Moscova, 1979.

Loper C.R., Heine R.W., *Graphite Formation During Solidification of Cast Iron.* Modern Casting, Noiembrie 1961, 117-134.

Loper C.R., Heine R.W., *The Solidification of Cast Iron with Spheroidal Graphite.* A.S.M. Trans., 1963, 135-152.

IPOTEZĂ ASUPRA MECANISMULUI FORMĂRII GRAFITULUI NODULAR UTILIZÂND CA MODIFICATOR MAGNEZIUL

(Rezumat)

Se prezintă modificarea fontei utilizând ca modificator magneziul. Din momentul în care s-au format bulele în fonta lichidă, procesul de difuzie al particulelor de carbon dinspre matricea metalică înspre bulele de magneziu, începe . Aglomerările de atomi de carbon din yona interfeței matrice metalică formează nuclee de grafit.Aceşti

nuclei încep să crească în bulele de magneziu şi, astfel, iau naştere monocristalele de grafit. Agregatul policristalin de grafit produs are acelaşi volum ca şi bula de magneziu în care a crescut şi se numeşte nodul de grafit – grafit nodular, grafit globular sau grafit sferoidal.

BULETINUL INSTITUTULUI POLITEHNIC DIN IAŞI
Publicat de
Universitatea Tehnică „Gheorghe Asachi” din Iaşi
Tomul LIX (LXIII), Fasc. 1, 2013
Secţia
ŞTIINŢA ŞI INGINERIA MATERIALELOR

CONSIDERATIONS REGARDING THE PHYSICAL METALLURGY OF Ti-BASED ALLOYS FOR DENTAL PROSTHETICS

BY

**MARIA BACIU[1,*], ELENA-RALUCA BACIU [2], IRINA GRĂDINARU[2]
and NORINA-CONSUELA FORNA[3]**

[1]“Gheorghe Asachi” Technical University of Iaşi
Department of Material Engineering and Industrial Security,
“Gr. T. Popa” University of Medicine and Pharmacy of Iaşi,
[2]Department of Dental Materials,
[3]Department of EPI Clinic and therapy

Received: February 28, 2012
Accepted for publication: March 7, 2012

Abstract: The prosthetic restorations have a complex construction in whose structure there are numerous metal components. Ti-Al-Nb alloys may be analysed by means of binary balance diagrams Ti-Al, Ti-Nb and Al-Nb or by means of isothermal sections made into the ternary diagram. The properties of the elements from the chemical composition will exert their influence on the physical, mechanical and technologic properties of formed alloys.

Keywords: prosthetic restoration; Ti-based alloys; balance diagrams.

1. Introduction

Prosthetic restorations specific to the dental medicine have a complex construction in whose structure there are numerous metal components. Each metal component from the structure of prosthetic restorations has its functional role, own geometry and specific making technology. The fulfillment of these

---

[*]Corresponding author: *e-mail*: maria_baciu2004@yahoo.co.uk

conditions must take into account an essential criterion: the one represented by the choice of material.

The behaviour of dental alloys in the melting solidification processes may be analysed by means of isothermal sections traced through the ternary balance diagrams or by means of constitutive binary diagrams.

2. Goal of the Study

The study aims at characterizing the Ti-based dental alloys for the mobile prosthetic restorations from the viewpoint of the balance structure and chemical composition.

3. Material and Method

Taking into consideration the recommendations presented in the specialized scientific literature as well as the results from the practical experience of the dental labs, we have analysed the following two materials Biotan™ Titanium and Biotan™-Nb (Schütz Dental GmbH) for the metal components of the skeletal removable partial denture and fixed prosthetic restorations (Table 1).

Table 1
Non-Noble Dental Alloys under Analysis

Class of materials	Material brands	Producer	Use recommendations
Titanium-based alloys	Biotan ™ Titanium	Schütz Dental GmbH (Germany)	– skeletal prostheses with grooves and special systems; – bridges; – superstructures
	Biotan ™-Nb, (Ti-6Al-7Nb)	Schütz Dental GmbH (Germany)	– skeletons, simple groves, clasps, – metallic-ceramic bridges

4. Results. Discussions

Ti-Al-Nb alloys may be analysed by means of Ti-Al, Ti-Nb and Al-Nb binary balance diagrams (Fig. 1) or by means of isotheral sections made into the ternary diagram. At the room temperature, Ti-6Al-7Nb alloy has a biphasic structure ($\alpha + \beta$) it thus being susceptible to processing by thermo-mechanical treatments (Barbosa & Button, 2000).

For Ti-Al alloys (Fig. 1), we may notice that in small aluminum concentrations (Al < 12%), the basic metal base has a monophasic character being made of a solid solution rich in (Ti_{α}). For higher aluminum content, intermetallic compound Ti_3Al will also be present in the structure with a hardening effect of the metal matrix (Watanabe *et al.*, 2003).

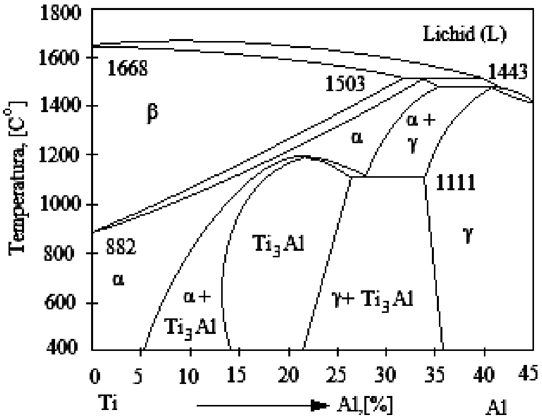

Fig. 1 – Balance diagram of Ti-Al alloy system.

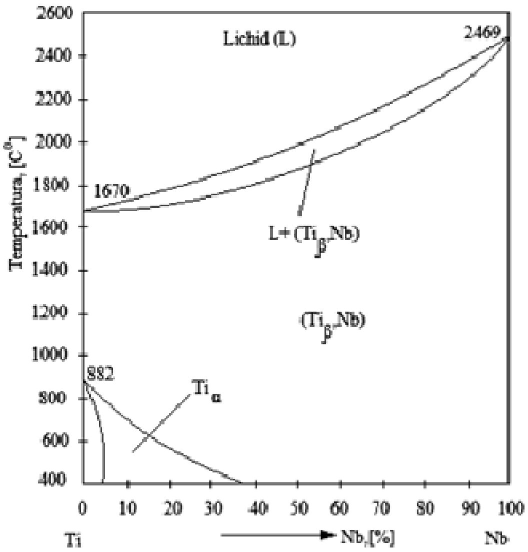

Fig. 2 – Balance diagram of Ti-Nb alloy system.

In case of Ti-Nb binary alloys, at low temperatures and concentrations below 37% Nb, the structure will be made of a Ti_α-based solid solution (Fig. 2) (Moffat & Kattner, 2006). For values of aluminum lower than 10%, the structure of Nb-Al alloys will be represented by a niobium-based phase of solid solution type (Fig. 3). In case of higher quantities of aluminum, intermetallic compounds Nb_3Al, Nb_2Al and Al_3Nb will form and their presence will influence the properties of alloys (Chlebus, *et al*., 2011).

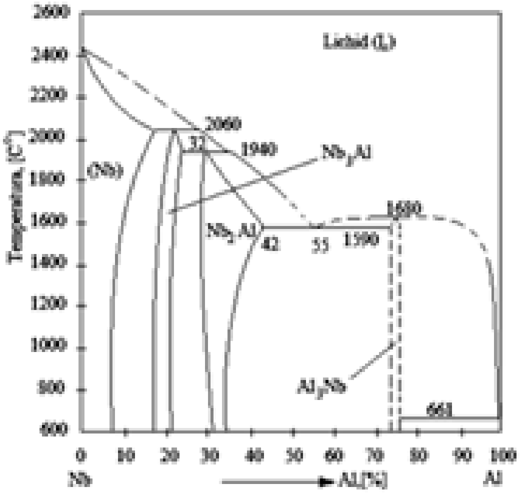

Fig. 3 – Balance diagram of Nb-Al alloy system.

The non-noble dental alloys under analysis were purchased from the manufacturing companies and they have established values for the chemical composition, physical and mechanical properties, pursuant to the technical sheets of the product (www.schűtz-dental.de).

As for the chemical composition, we may notice that Biotan™Nb is a complex Ti-based alloy as compared to Biotan™ Titanium which is an alloy of technical purity (Table 2).

Table 2
Chemical Composition of Ti-Based Alloys

Alloy brand	Chemical composition, [%]											Technical norm
	Co	Ni	Cr	Mo	Ti	Nb	Al	W	Si	Mn	C	
Biotan™ Titanium	–	–	–	–	99.5	–	–	–	–	–	–	ASTM B 265 (Gr.1,2,3,4)
Biotan™ Nb	–	–	–	–	87	7.24	6.28	–	–	–	<0.08	ISO 9693: 2000 ISO 5832-3 ASTM F1295

The properties of elements within the chemical composition will exert their influence on the physical properties of the alloys formed, Table 3.

Table 3
Physical Properties of the Ti-Based Alloys

Alloy brand	Density, g/cm^3	Melting temperature °C	Casting temperature °C	Dilatation coefficient α (25°...600°C) K^{-1}	Colour
Biotan ™ Titanium	4.5	1,668	–	–	–
Biotan™ Nb	4.52	1,650	–	–	–

In correlation with the chemical composition, it is obvious that the Ti-based alloys selected require higher melting and casting temperatures, a fact which requires that their processing by casting should need vacuum melting special equipment or inert atmospheres so as to mainly avoid the oxidization process.

An important role in the evaluation of technological processability by chipping, plastic deformation or welding etc. and of behaviour during use of the metal components made is played by the mechanical resistance properties (R_m and $R_{p0,2}$), plasticity (A_5 and E) and the hardness of the alloys used (Table 4).

Table 4
Mechanical Properties of Ti-Based Alloys

Alloy brand	Breaking strength, R_m, [MPa]	Proportionality limit, $R_{p0,2}$ MPa	Elongation A_5, [%]	Microhardness HV$_{10}$	Elasticity module, E GPa
Biotan ™ Titanium	600...680	500...530	24	220	95
Biotan™ Nb	850...900	1,000	14.5	325	110

5. Conclusions

1. For the evaluation of technological processability of alloys, mainly of the processing by chipping, an important role is played by the mechanical properties of strength, plasticity and hardness specific to each material.

2. According to the balance diagram of Ti-Al-Nb system, a biphasic structure (α + β) will correspond to Ti-6Al-7Nb alloy it thus being susceptible to processing by thermo-mechanical treatments.

3. The presence of Ti_3Al intermetallic compound in the structure of Ti-Al-based alloys has as an effect the increase of the strength mechanical characteristics.

4. As for the chemical composition, we may notice that Biotan™Nb is a complex Ti-based alloy as compared to Biotan™ Titanium which is an alloy of technical purity.

REFERENCES

Barbosa P.F., Button S.T., *Microstructure and Mechanical Behaviour of the Isothermally Forged Ti-6Al-7Nb Alloy*. Proc. of the Inst. of Mechan. Eng., Part L: J. of Mater.: Design a. Appl., 2000, http://pil.sagepub.com/content/214/1/23.

Chlebus E., Kuznicka Bogumila, Kurzynowski T., Dybala B., *Microstructure and Mechanical Behaviour of Ti-6Al-7Nb Alloy Produced by Selective Laser Metting*. Materials Characterization, **62**, *5*, 488-495 (2011).

Moffat D.L., Kattner U.R., *The Stable and Metastable Ti-Nb Phase Diagrams*. Metallurgical and Materials Transaction A, **19**, *10*, 2389-2397 (2006).

Watanabe K., Miyakawa O., Takada Y., Okuno O., Okabe T., *Casting Behaviour of Titanium Alloys in a Centrifugal Casting*. Biomaterials, **24**, *3*, 1737-1743 (2003).

* * * *Binary phase diagram of Al-Nb*. Illinois Inst of Technol., http://tptc:űt.edu/ index.php/option=com.content&view, last updated, 06.08.2010.

* * * *Biotan ™ Titanium*. Schűtz Dental Group, Catalogue, 2010, 41, www.schűtz-dental.de.

CONSIDERAȚII PRIVIND METALURGIA FIZICĂ A ALIAJELOR PE BAZĂ DE Ti DESTINATE PROTETICII DENTARE

(Rezumat)

Restaurările protetice au o construcție complexă, în structura cărora se regăsesc numeroase componente metalice. Aliajele Ti-Al-Nb pot fi analizate cu ajutorul diagramelor de echilibru binare Ti-Al, Ti-Nb şi Al-Nb sau prin intermediul secțiunilor izoterme efectuate în diagrama ternară. Proprietățile elementelor din compoziția chimică îşi vor exercita influența asupra proprietăților fizice, mecanice şi tehnologice ale aliajelor formate.

BULETINUL INSTITUTULUI POLITEHNIC DIN IAŞI
Publicat de
Universitatea Tehnică „Gheorghe Asachi” din Iaşi
Tomul LIX (LXIII), Fasc. 1, 2013
Secţia
ŞTIINŢA ŞI INGINERIA MATERIALELOR

STUDY REGARDING THE INFLUENCE OF VIBRATIONS ON THE ALLOY 95% Al, 4.5% Cu, 0.14% Fe, 0.28% Si

BY

GELU BARBU[*]

“Gheorghe Asachi” Technical University of Iaşi
Department of Material Engineering and Industrial Security

Received: February 28, 2012
Accepted for publication: March 7, 2012

Abstract: Pure aluminum and its alloys-phase (consisting of aluminum-rich solid solution) have a very strong tendency towards the formation of large grain structure in castings and also to develop pronounced. For this reason the use of great practical importance vibrated for these alloys, allowing getting into ingots and castings of a fine-grained microstructure and a uniform macrostructures. This paper presents the results obtained for an alloy 95% Al, 4.5% Cu, 0.14% Fe and 0.28% Si.

Keywords: circular; horizontal vibrations; hardness; aluminum-alloys.

1. Introduction

There have been a number of specimens that were studied to observe the effect vibrated with an installation made circular, horizontal vibration patented in Romania

For the experiments we used the aluminum-silicon alloy containing 95% Al, 4.5% Cu, 0.14% Fe, 0.28% Si. For development we used an electric oven with resistors, using pure metals, alloys and master alloys previously developed liquid bath is protected with a layer of fondant.

---

[*] *e-mail*: barbugelu1234@yahoo.com

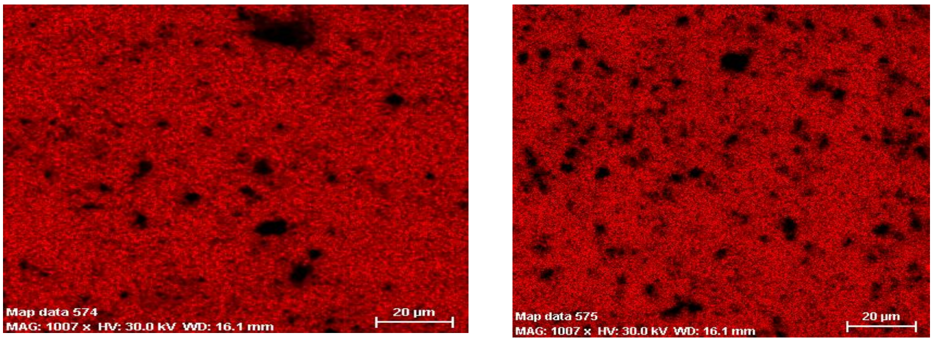

Sample 1 (vibrated) Aluminum diffusion Sample 2 (static)Aluminum diffusion

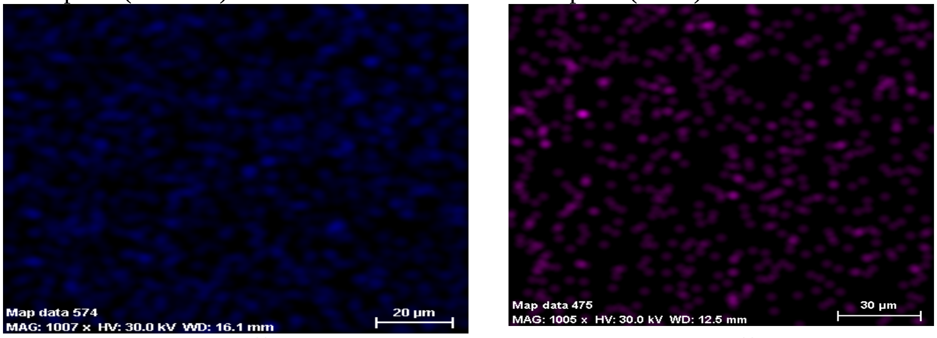

Copper diffusion Copper diffusion

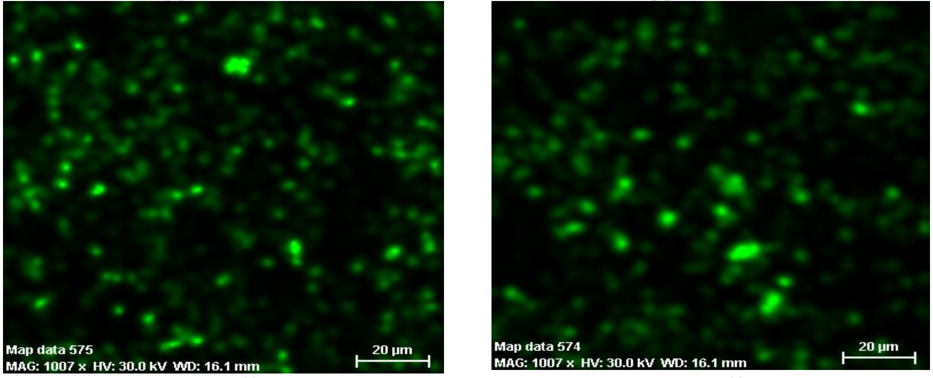

Silicon diffusion Silicon diffusion

Fig. 1 – The distribution of elements in the alloy of the samples 1 and 2 of circular cross section.

The casting temperature was 700°C, and the forms have been preheated to a temperature of approx. 100°C.

Dimensions and shape of the specimens are Φ50 × 100mm.

Circular section, circular, horizontal vibration promotes the movement of the alloy and it is cooled in an area deeper than the range which leads to a mixing and chemical composition.

Molded samples of an alloy of 95% Al, 4.5% Cu, 0.14% Fe, 0.28% Si were rated as follows:

a) Sample 1 – specimen with circular - casting vibrator;

b) Sample 2 – specimen with static casting;

They were sectioned specimens and samples that were subjected to EDAX spectometrer type maping. The EDAX analysis identified a flat copper or silicon in the alloy composition as shown in the Fig. 1 and spectrum in the Fig. 2.

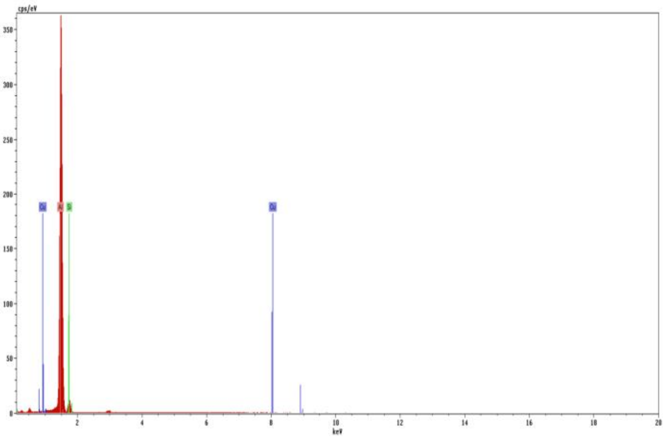

Sample 1 (vibrated)

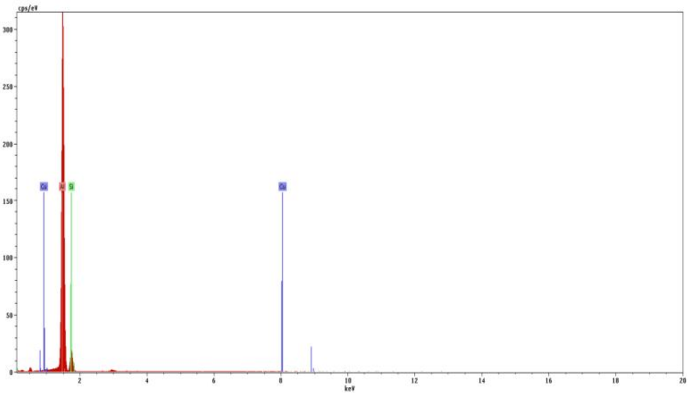

Sample 2 (static)

Fig. 2 – Samples 1 and 2 of circular-spectrum

They were sectioned specimens and samples that were subject to breakage, studying with the electron microscopy shape and dimensions of the rupture. Tears form shows a ductile fracture, attending cups and cones areas and areas where traces of sliding structures. Also as a result of requests made of small cracks can be observed intercrystalline. Rupture occurred transgranular and intergranular. These are described in Figs. 3 and 4.

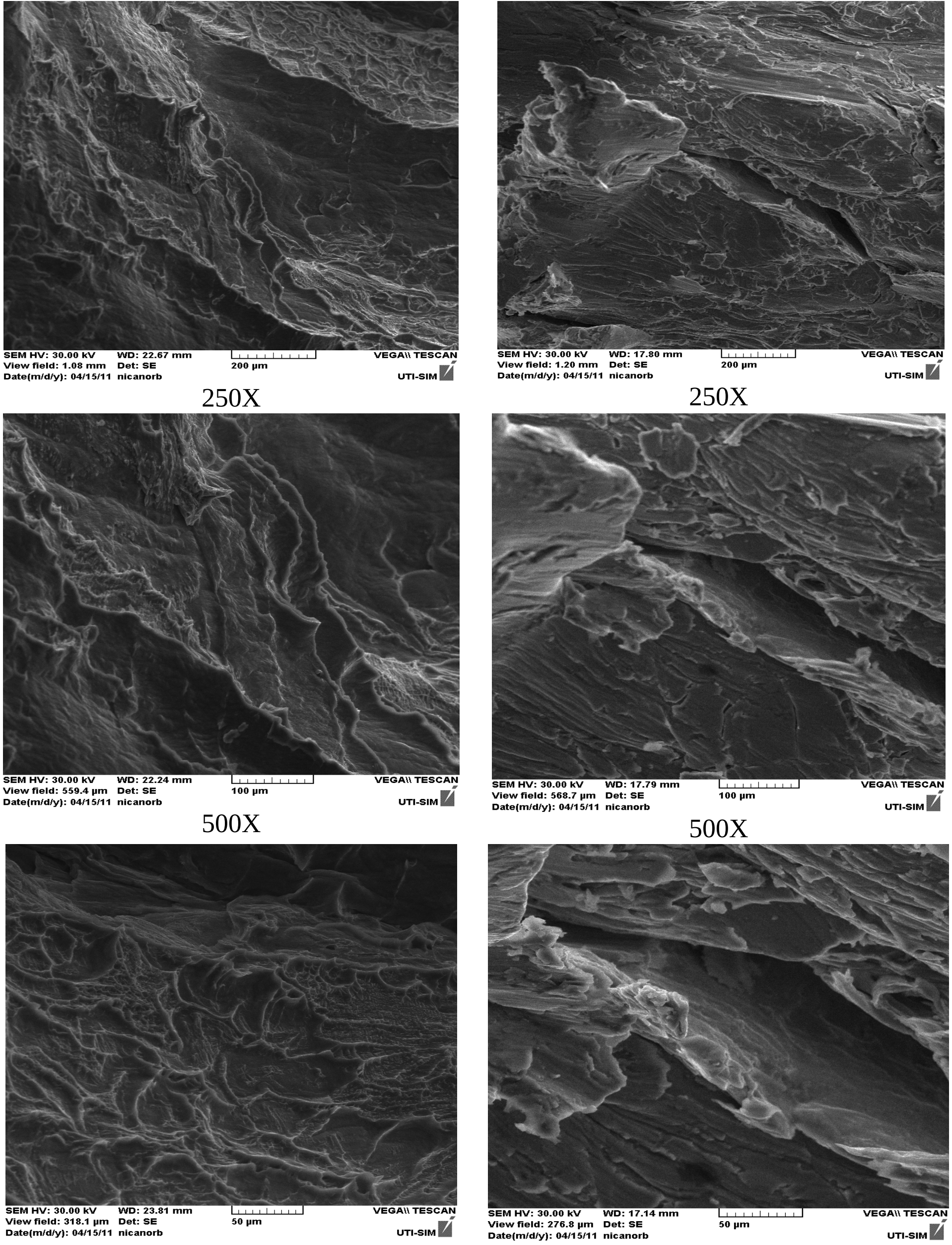
Sample 1 (vibrated)

Sample 2 (static)

250X 250X

500X 500X

1000X 1000X

Fig. 3 – Samples 1 and 2 of circular-section SEM.

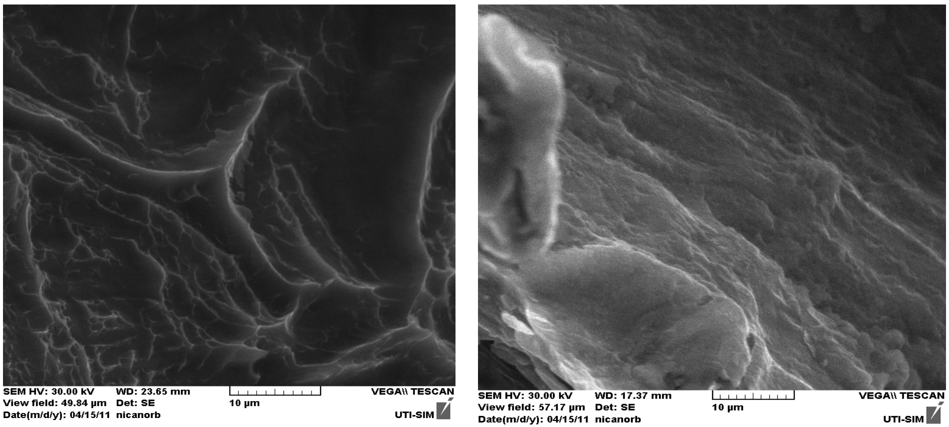

5000X 5000X

Fig. 4 – Samples 1 and 2 of circular-section SEM.

Hardness distribution was studied on longitudinal sections of the samples with a square section cylinder type universal hardness tester Wolpert Wilson 751N model was used as a method of determining the hardness, Brinell method for determination using a 2.5 mm ball penetrator using a task push the 62 kg force. The influence is marked on the sample with a circular cross-section where the rotation of the alloy is more intense.

The results of the test are shown in Table 1 for vibrated sample, and static cast in Table 2.

Table 1
Hardness Test 1

Hardness test 1 circular plate vibrating, [HB]					
29.22	31.34	32.81		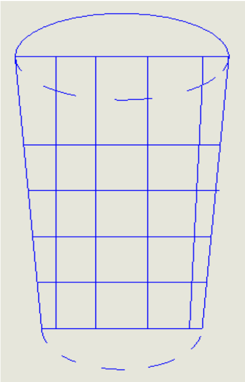	31.12
27.92	31.86	34.7			31.49
29.33	31.41	31.32			30.69
28.18	33.56	31.76	32.91		31.60
30.92	31.68	32.25	34.34		32.30
	23.98	36.88	31.34		30.73
29.11	30.64	33.29	32.86		average

Table 2

Hardness Test 2

Hardness test 2 static cast circular, [HB]					
30.58	27.34	29.66	35.84	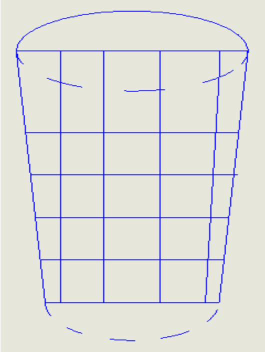	30.86
26.38	30.06	27	35.65		29.77
27.88	33.16	24.05	32.11		29.30
	34.23	27.69			30.96
	29.83	31.06			30.45
	31.16	32.6			31.88
28.28	30.96	28.68	34.53		average

The results of the hardness test are shown graphically in Figs. 5 and 6 in the longitudinal direction and transverse.

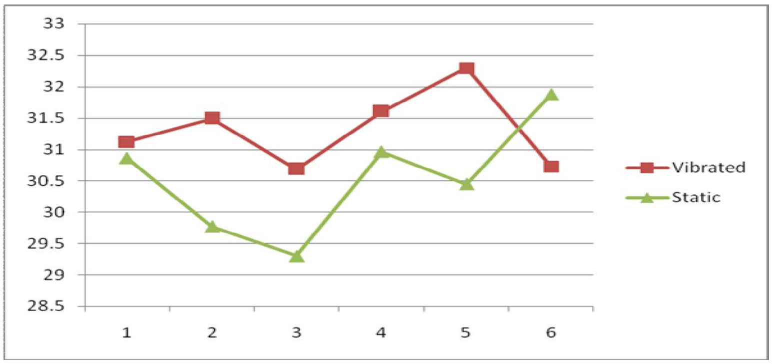

Fig. 5 – Chart hardness for samples.

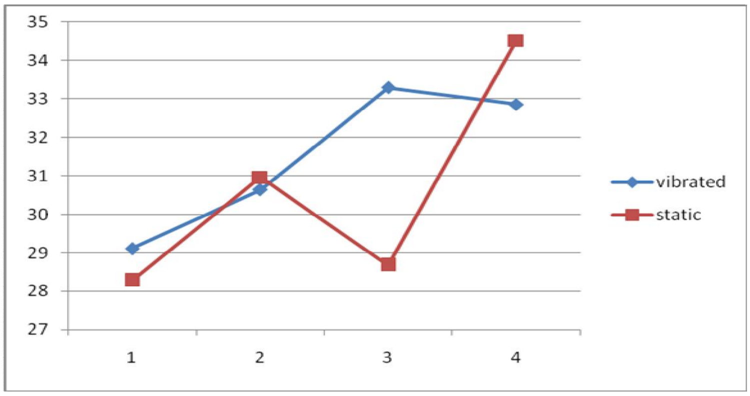

Fig. 6 – Chart hardness for samples with circular shape.

To highlight the fine grain of the alloy samples were prepared that were prepared to be subjected to chemical attack normally. The reagent has been used in chemical attack has the following composition: 0.5 ml HF, 1.5 HCl, 2.5 ml NH3, 95.5 distilled water. Following the attack samples were studied using electron microscopy, Fig. 7, the structures seen within grains seeing a finer structure for samples and hence vibrate a uniformity of material properties.

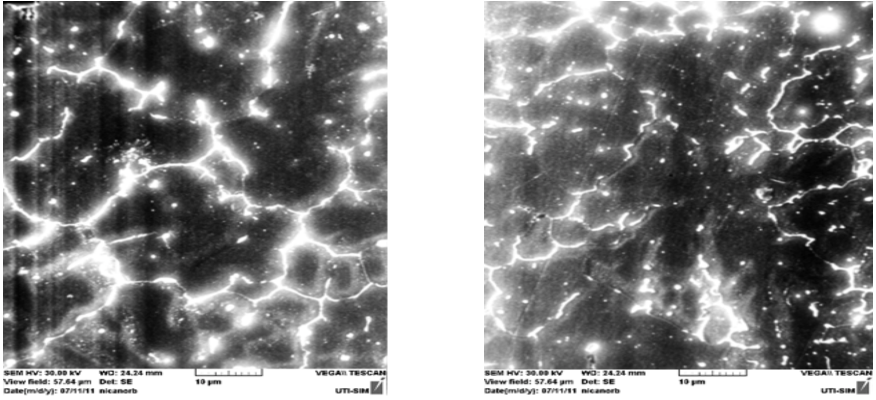

Sample 2 (static) — 300X

Sample 1(vibrated) — 300X

Fig. 7 – Structures samples.

2. Conclusions

According to EDAX analysis identified a uniform distribution of alloy elements for horizontal circular vibrating molded specimens.

It can be seen in most of the finer structural failure in the test specimens being subjected to vibration during solidification, which demonstrates the beneficial effect on the grain structure.

Tears form shows a ductile fracture, attending cups and cones areas and areas where traces of sliding structures. Also as a result of requests made of small cracks can be observed intercrystalline. Rupture occurred transgranular and intergranular.

Microscopy done on samples of chemical attack structure is observed in grain boundaries. If there is a vibrating sample finer structure and hence the uniformity of material properties.

REFERENCES

Barbu G.,Cojocaru V., Carcea I., *Instalație de turnare cu vibrare*. Brevet invenție România, *108934B1*/1994;

Buzdugan Gh., *Vibrațiile sistemelor mecanice*. Ed. Academiei, Bucureşti, 1970.

Hoffman R., *Mold Having Heating and Vibration Means.* United States Patent Office, *3.506.062*, 14.04.1970.

Jayesh Deshpande, *The Effect of Mechanical Mold Vibration on the Characteristics of Aluminium Alloys*. Worcester Polytechnic Institute, September 2006.

Şontea S., Vlădoi M., Zaharia N., *Metale şi aliaje neferoase de turnătorie*. Ed. Scrisul românesc, Craiova 1981.

Ştefănescu Fl., Bratu C., *Cercetări privind influenţa vibrării asupra compactităţii aliajelor turnate*. Metalurgia, *5*, 1985.

Ştefănescu Fl., *Procese fizice care au loc la vibrarea aliajelor turnate. Efecte tehnologice. Principii de proiectare a instalaţiilor de turnare*. Metalurgia, *9*, 1987.

STUDII PRIVIND INFLUENŢA VIBRAŢIILOR ASUPRA UNUI ALIAJ CU 95% Al, 4.5% Cu, 0.14% Fe, 0.28% Si

(Rezumat)

Aluminiul şi aliajele sale (constând din aluminiu-bogat în soluţie solidă) au o tendinţă foarte puternică de formare a unei structuri granulare grosolane în piesele turnate. Din acest motiv, utilizarea vibrării are mare importanţă practică pentru aceste aliaje, permiţând obţinerea unei microstructuri cu granulaţie fină şi uniforme lingouri şi piese turnate. În lucrare sunt prezentate rezultatele obţinute pentru un aliaj 95% Al, 4,5% Cu, 0,14% Fe si 0,28% Si.

BULETINUL INSTITUTULUI POLITEHNIC DIN IAŞI
Publicat de
Universitatea Tehnică „Gheorghe Asachi” din Iaşi
Tomul LIX (LXIII), Fasc. 1, 2013
Secţia
ŞTIINŢA ŞI INGINERIA MATERIALELOR

CONSIDERATIONS ON SUPERCONDUCTING LIMIT SWITCHES

BY

VASILE BAHRIN[*]

“Gheorghe Asachi” Technical University of Iaşi
Faculty of Electrical Engineering

Received: February 28, 2012
Accepted for publication: March 7, 2012

Abstract: The paper presents the specific features of superconducting materials related to the phase transition normal state-superconducting state and the properties for type I and type II superconductors. In this context, it is addressed the operation principle of superconducting limiters and there are highlighted the differences between these devices and the classical ones.

Keywords: superconductivity; resistance transition; phase transition.

1. Introduction

The superconducting a.c. limit switch. constitutes an application of superconductivity, it is intended to cut any current that exceeds a required value and has no voltage limit. The usual devices (circuit breakers), interrupt the current when it passes through zero. Using the superconducting current limit switch in a power network leads to improved operation by increasing the dynamic stability, the maximum transmission power and interconnectivity for a better quality of electricity. Superconducting limit switch are based on natural and ultra rapid transition from superconducting state to a dissipative state

---

[*] *e-mail*: vasilebahrin@yahoo.com

(normal) by overcoming the critical current and integrates detection, control and active part. Operation of this limitation is very rapid (μs) and repetitive, the superconducting state being recovered in a few seconds after being isolated from the network via a classic circuit breaker.

2. Resistance Transition of the Superconducting Material

The superconducting material is characterized by a resistance transition between normal and superconducting state. This transition can be induced by overcoming a critical value of a physical quantity: the critical temperature, T_c, critical field, H_c, or the critical current density, J_c. After propagation onset transition propagation takes place due to Joule effect induced locally in the superconducting material, or may be controlled.

Resistance transition by overcoming critical temperature is used for superconducting circuit breakers and less for current switch due to time constants of heating and insulation problems that would arise by insertion of a heating element.

Applying a pulse of magnetic field greater than the critical field, facilitates obtaining the superconductor transition. This technique is used to force the transition of massive bars with high superconducting critical temperature, which have a characteristic $J_c = f(B)$ very sensitive to magnetic induction, B. In the case of industrial superconductors with low critical temperature, critical fields imply significant control systems.

Transition by overcoming current critical is the principle at the base of the superconducting current limit switch systems and does not require detection or control. The line current has the triggering role for current limitation and the modification of conductor cross section determines at calibration the current threshold (Bashkirov *et al*., 1995).

When current density exceeds the critical current density the superconductive material is not directly in normal status, but in an intermediate disipative state. In these circumstances, in the case of low critical temperature superconductors can occur a heat packing, leading to overpassing the critical temperature.

High critical temperature superconductors (HTS) have high volumetric heat capacity (Table 1) and can be used in bulk without stability loss (Tixador, 1998). The resistivity of these superconductors presents the particularity that is is not required a complete transition for the limiting effect to occur. Under these conditions results a weak dissipation with recovery times compatible with automatic closing cycles of circuit breaker (OCO-cycle: open-closed-open).

It is considered that the “flux flow” state is the moment when overcoming the critical current density, appears a movement of fluxoids characteristic to HTS supraconductors (type II) with an appearance of “stream flow” resistance, rff, intermediate between that of the normal state and that null one of the superconducting state. One notes that the resulting heat is not enough to make the superconductor to transit and the “flux flow” can be stable. Some materials with low current density (such as non-textured YBaCuO) may have this stable state when critical current is greatly overcome. Compared with these materials, textured materials or bismuth compounds that have volumetric loss ($\rho_{ff} J_c^2 = 2\times10^{10}\ \mathrm{W\cdot m^{-3}}$), 100 times larger reach fast enough the normal state.

Table 1

Material Properties of High-(HTS) and Low (LTS) Critical Temperature

Characteristics	HTS	LTS
Resistivity in normal state ρ_n, [Ω·m]	10^{-5}	4×10^{-7}
Thermal conductivity (at T_c) λ, [W· m^{-1}· K^{-1}]	9	0.3
Critical current density in superconductor J_c(supr), [A·m^{-2}]	5×10^8	10^{10}
Critical current density J_c(overall), [A·m^{-2}]	2×10^8	2×10^9
Volume thermal capacity: C, [J·m^{-3}·K^{-1}]	10^6	5,000
Thermal diffusion coefficient D_{th}, [m^2 · s^{-1}]	9×10^{-6}	6×10^{-5}
Entalpy variation between T_0 and 300 K $\Delta H\ \Big]_{T_0}^{300K}$, [$J$·m^{-3}]	4×10^8	7×10^8
ρJ_c (overall), [V·m^{-1}]	2,000	800
ρJ_c^2 (overall), [V·m^{-3}]	4×10^{11}	1.6×10^{12}
$\left.\dfrac{\rho J_c^2}{c}\right]_{t=0}$, [K·s^{-1}]	4×10^5	3.2×10^8
Propagation speed: V_p, [m·s^{-1}]	0.7	100

Phenomenon caused by heat activating the movement of flux lines (called “flux creep”) is important for HTS superconductors and negligible if LTS ones. When operating temperature is close to the critical temperature, this phenomenon changes the behavior in time of HTS materials.

The effect of heterogeneity and accumulation of particles are very important for these materials. Critical current density, J_c, corresponds to the appearance of a voltage of $0.1\,\mu$V.cm^{-1}. Over this value the flux lines are moving, but not associated dissipation superconductor to transit in normal status.

For $J > J_0 \approx J_0^{'}(T_c - T)$ during the “flux flow” state the following relation exists between voltage and current density (Fig. 1).

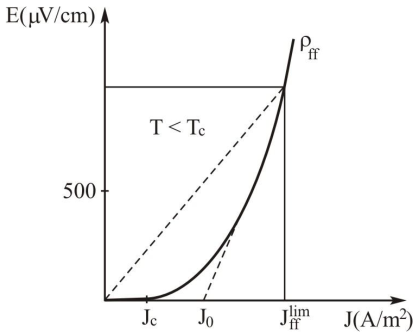

Fig. 1 – “*Flux low*” resistivity.

Current may be limited with a resistivity lower that the limiting resistivity $\rho_n(T)$ in the normal state which would occur if $T > T_c$..

Time required to achieve normal state is given by (Tixador, 1998; Gyore *et al*., 2009):

$$\Delta t \approx \int_{T_0}^{T_c} \frac{C(T)}{J\,E(J,T)} \mathrm{d}\,T \,. \qquad (1)$$

For LTS materials, the low volumetric heat capacity $C(T)$ and dissipated density of energy JE lead to overcoming the critical temperature within a few μs, and the HTS are necessary for several ms (http://www.super-conductors.org/).

3. Conclusions

The impedances rates of the superconducting limit switch must have the value: $Z_{\text{fault}}/Z_{\text{nom}} >> 1$.

In building a current limit switch we must take into consideration:

a) automatic operation, without additional system of detection and control;

b) limitation of first current peak is in less than 2…3 ms (< 1/4 period), which implies very low impedance, voltage drop and loss, concomitant with signal quality (lack of harmonics);

c) introduction of a high impedance and limited heating in the faulty regime;

d) transition from the normal state of the faulty one should not be accompanied by discontinuities which could favor overvoltages or transient overcurrents;

e) fast-recovery to a normal state for a good continuity in the operation;

f) safe operation, limited impact in the event of incorrect operation, low weight and occupied space.

To eliminate the faults and isolation of fault zones a breaking element is connected in series, calibrated according to the rated current ($3…5I_{nom}$) to avoid sudden disruptions due to transitional arrangements or regimes defect.

Compared with the classical devices, the superconducting current limit switch presents many advantages:

a) immediate current limiting, which provide protection against the electromagnetic stress due to overcurrents;

b) self-functioning, natural and repetitive, the transition from the superconducting to normal state being performed an unlimited number of times;

c) under normal operation the losses and voltage drops are low;

d) self protection in the case of refrigeration stop by superconductor shift to normal state;

e) compatible with the requirements of a higher quality of supplied electricity.

The disadvantages of superconducting current limit switches are given by the high investment, the existence associated cryogenic equipment, compatibility and interconnection with the network (current paths).

REFERENCES

Bashkirov A.Yu., Yakimets V.I., Fleishman S.L., Narovlyanskii G.V., *Application of Superconducting Shields in Current-Limiting and Special-Purpose Transformers.* IEEE Trans. on Appl. Superconductivity, **5**, *2*, 1075-1078, 1995.

Tixador P., *Les supraconducteors.* Edit. HERMES, Paris, France, 1998.

Gyore A., Vajda I., Meerovich V., Sokolovsky V., *Experimental Determination of Optimal Construction of Current Limiting Transformers Using HTS Tapes and Rings.* IEEE Trans. on Appl. Superconductivity, **19**, *3*, 1976-1980, 2009.

* * * http://www.superconductors.org/.

CONSIDERAŢII ASUPRA LIMITATOARELOR SUPRACONDUCTOARE

(Rezumat)

Sunt prezentate particularităţi ale materialelor supraconductoare legate de tranziţia de fază stare normală-stare supraconductoare, precum şi proprietăţi ale acestora în cazul supraconductoarelor de tip I şi tip II. În acest context, se abordează principiul de funcţionare al limitatoarelor supraconductoare şi se evidenţiază deosebirile lor faţă de cele clasice.

BULETINUL INSTITUTULUI POLITEHNIC DIN IAŞI
Publicat de
Universitatea Tehnică „Gheorghe Asachi” din Iaşi
Tomul LIX (LXIII), Fasc. 1, 2013
Secţia
ŞTIINŢA ŞI INGINERIA MATERIALELOR

OPTIMIZATION OF THE MECHATRONIC HYDRAULIC SYSTEM PARAMETERS BY THE METHOD OF GENETIC ALGORITHM

BY

V. STRUTINSKIY[1,*], Y. BURENNIKOV[2] and L. KOZLOV[2]

[1]Kyiv National Technical University, Ukraine,
[2]Vinnytsia National Technical University, Ukraine

Received: February 28, 2012
Accepted for publication: March 7, 2012

Abstract: The paper considers a mechatronic hydraulic system based on a variable pump, a hydraulic cylinder, a proportional directional control valve, a system of sensors and a controller. The hydraulic system provides regulation and stabilization of the hydraulic cylinder piston motion speed within a wide range of load variations. In the process of its operation the controller implements the function of PD regulator with automatic adjustment of the differential component coefficient by means of a neural network. A non-liner mathematical model of the mechatronic hydraulic system has been developed. The mathematical model equations are solved in MATLAB-Simulink software environment. Using the method of genetic algorithm, values of the inclination angle α_p for the working edge of the pump regulator spool and the pump regulator throttle area f_0 have been found as well as the pump servocylinder throttle area f_e which provides the required response t_p = 0.22 s of the mechatronic hydraulic system for the hydraulic cylinder load variations within the range of $N = (0 - 10) \times 10^3$ N and the pump flow rate variations within the range of $Q = (0 - 10) \times 10^{-3}$ m^3/s.

Keywords: mechatronic system; manipulator; controller; mathematical model; genetic algorithm; optimization.

---

[*]Corresponding author: *e-mail*: sophiayablonskaya@gmail.com

1. Introduction

Hydraulic manipulators have been increasingly used in modern industry. Hydraulic manipulators are equipped with different-purpose grippers. Their operation is characterized by frequent changes in the modes of the hydraulic manipulator motion. Under such conditions the manipulator hydraulic system must provide minimization of energy consumption during the operation cycle as well as the required static and dynamic characteristics (Kozlov, 2012).

2. Optimization of the Mechatronic System

For solving this problem a mechatronic hydraulic system is proposed. The system is based on a variable pump, directional proportional control valve and analog-digital regulator with a neural controller (Fig. 1).

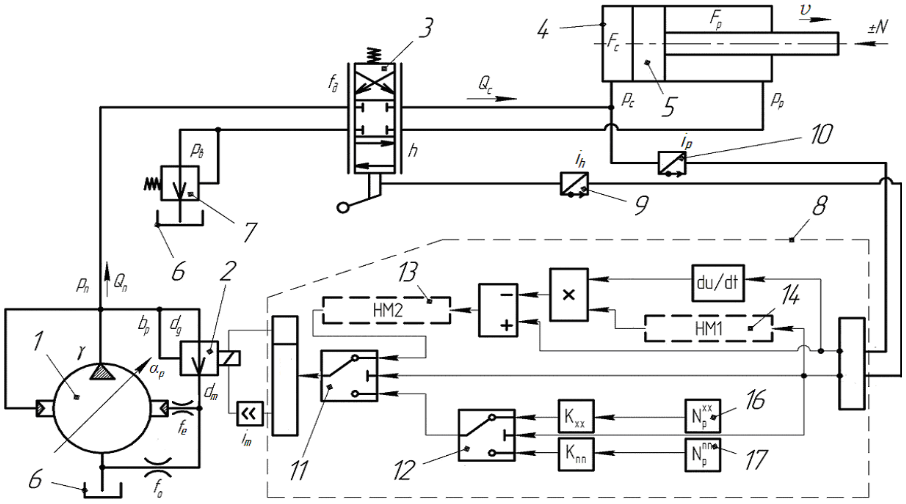

Fig. 1 – Mechatronic hydraulic system with digital regulator on the basis of a neural controller.

The mechatronic hydraulic system includes variable pump *1* with regulator *2*, proportional directional control valve *3*, hydraulic cylinder *4* with piston *5*, hydraulic tank *6*, pressure compensator *7*, controller *8*, displacement sensors *9* and pressure sensor *10*.

Controller *8* implements functions of a digital regulator in the mechatronic hydraulic system. It includes logic units *11*, *12* and networks *13*, *14*.

The mechatronic hydraulic system operates in the following way. Flow rate Q_n from pump *1* is supplied to hydraulic cylinder *4* through directional control valve *3* to hydraulic cylinder *4* and activates its piston. Working fluid from the hydraulic cylinder is discharged to hydraulic tank *6* through proportional directional control valve *3* and pressure compensator *7*. Displacement sensor *9* registers position h of the spool of directional control valve *3* and sensor *10* registers the value of pressure p_c at the input of hydraulic cylinder *4*. Signals from sensors *9* and *10* are supplied to controller *8* that forms control signal i_m for the proportional solenoid of regulator *2*. When the value of h of the directional valve spool position changes, the value of flow rate Q_c , that flows from pump *1* to hydraulic cylinder *4*, will be changing proportionally. The value of flow rate Q_n and, respectively, motion speed v of the hydraulic cylinder piston do not depend on the direction of the load N acting on hydraulic cylinder *4*. Pressure compensator *7* provides stabilization of speed v of the hydraulic cylinder piston motion when there is a concurrent load.

Digital regulator provides the hydraulic system operation in the idle mode, in the modes of constant flow, overload protection, hydraulic cylinder speed control modes under counter load and concurrent load conditions.

When proportional directional control valve is closed, $h = 0$ (the idle mode), and flow rate from pump *1* is not supplied to hydraulic cylinder *4*, piston *5* of hydraulic cylinder *4* is in a fixed position. Pump *1* supplies small flow rate Q_n to the hydraulic system that provides its control system operation. The digital controller with the help of units *11*, *12* and *16* together with generator *2* will maintain pressure p_n = 1.5 MPa at the pump output. Unproductive power losses in the idle mode are inconsiderable.

For maximal opening $h_{\max}$ of proportional directional control valve *3* pressure p_n at the output of pump *1* will depend on load N at hydraulic cylinder *4*. The digital controller with the help of units *11*, *12*, *17* and regulator *2* will limit pressure $p_{n\,\max}$ to the value of 16.0 MPa, that is the maximal permissible value for a mechatronic hydraulic system. Flow rate Q_n , in this case, will be equal to the maximal productivity of the variable pump. The value of flow rate supplied to the hydraulic cylinder $Q_c = Q_n$ will not change and the piston of hydraulic cylinder *4* will move at a constant speed. In this way the constant flow and overload protection modes will be realized. Power losses in the constant flow mode are determined by pressure losses when flow rate Q_n of the working fluid is supplied from the pump to the hydraulic cylinder. In the overload protection mode unproductive power losses in the hydraulic system will be inconsiderable and will be determined by the working fluid flow rate required to support operation of regulator *2*, flow rate Q_n not being supplied to hydraulic cylinder *4*.

When opening h varies in the range of $0 \le h \le h_{\max}$ (hydraulic cylinder speed control mode) the digital controller maintains pressure differential

$\Delta p = p_n - p_c = 0.8$ MPa at the hydraulic cylinder with the help of neural network *13*, which enables proportional control of flow rate value Q_c to hydraulic cylinder *4* by changing the value of h. Flow rate Q_c and, therefore, motion speed v of piston *5* will remain stable under both counter load and concurrent load conditions. Under concurrent load conditions pressure p_n at the output of variable pump *1* will be determined by the setting of pressure compensator 7 and will be equal to 1.0 MPa. Under concurrent load conditions pressure p_n will depend on the value of load N at hydraulic cylinder *4*. With the increase of N pressure p_n will be growing to the value of $p_n = p_{n\,\max}$ = MPa determined by the digital controller setting. In the hydraulic cylinder speed control mode power losses will be inconsiderable. Since the flow rate Q_n of the variable pump will be close to the flow rate value Q_c , consumed by the hydraulic cylinder *4*, pressure value p_n will be proportional to the counter load value.

The digital controller includes PD regulator with automatic control of the differential component coefficient. Correction of the differential component coefficient is realized by neural network *14* depending on the opening value h of the proportional directional control valve. Use of PD regulator makes it possible to reduce the values of overshooting and regulation time in the mechatronic hydraulic system under dynamic modes (Rotkovskaia, 2006).

To provide the mechatronic hydraulic system operation, neural network *13* is used. It includes one input, one output and one hidden layer of six neurons. Neural network *13* is formed on the basis of neurons having activation function of a hyperbolic tangent type for the hidden layer of neurons and linear activation function for the output neuron.

In order to check functionality of the digital controller and to find optimal parameters of the hydraulic system, a nonlinear mathematical model has been developed. The mathematical model includes eq. (2) of torques at the faceplate of pump *1* (Fig. 1), equation of forces at piston *5* (eq. (1)), at the spool of regulator *2* (eq. (3)), at the spool of pressure compensator *7* (eq. (9)), flow continuity equation for hydraulic lines between pump *1* and directional proportional control valve *3* (eq. (4)), between proportional directional control valve *3* and hydraulic cylinder *4* (eq. (5)), between regulator *2* and the throttle in the control system of pump *2* (eq. (6)), between the damper in the control system of pump *1* and servoplunger of pump *1* (eq. (8)), between the damper of pressure compensator and its spool (eq. (10)), between hydraulic cylinder *4* and pressure compensator *7* (eq. (11)) as well as equation of voltage drop in the electromagnet circuit of regulator *2* (eq. (7)), dependences of the current value at the sensor output on the pressure value (eq. (13)), the flow rate value of pump *1* on the faceplate inclination angle (eq. (12)), the value of the total deformation rate of the working fluid and rubber-metal sleeves on the pressure (eq. (14)).

The mathematical model is built taking into account the following assumptions and simplifications: the hydraulic system lumped parameters are considered; the working fluid temperature is taken into account as a constant value; wave processes are not taken into account; coefficients of flow through throttle and spool elements are constant; operation modes are cavitation-free; the volume of hydraulic lines remains unchanged during transient processes; pressure losses in the hydraulic lines are not taken into account; dry friction forces do not depend on the speed of movable elements; operation of the controller was simulated by a proportional link with a time delay; direction of the load action at the hydraulic cylinder rod is unchanged; pressure losses in hydraulic cylinder *3*, when the working fluid is discharged from hydraulic cylinder *4*, are not taken into account.

$$\begin{aligned}I\frac{\mathrm{d}^2\gamma}{\mathrm{d}t^2} &= p_n f_5 l - p_e f_4 l - 2b_\gamma l\frac{\mathrm{d}\gamma}{\mathrm{d}t}\cos\gamma + 26.41 - 3.17\left(\frac{p_n - 9\times10^6}{7\times10^6}\right) - \\ &-9.86\left(\frac{Q_n - 0.67\times10^{-3}}{0.5\times10^{-3}}\right) - 2.2\left(\frac{p_n - 9\times10^6}{7\times10^6}\right)\left(\frac{Q_n - 0.67\times10^{-3}}{0.5\times10^{-3}}\right);\end{aligned} \tag{1}$$

$$m_c\frac{\mathrm{d}v}{\mathrm{d}t} = p_c F_c \pm N - \pi\left(q_0 + k_q p_c\right)\left(D_c + d_s\right)\mathrm{sign}v - p_p F_p; \tag{2}$$

$$m_p\frac{\mathrm{d}^2 z}{\mathrm{d}t^2} = p_n\frac{\pi d_g^2}{4} - k_m i_m - \left(\frac{\pi\rho v_k d_m l_p}{\varepsilon_p}\right)\frac{\mathrm{d}z}{\mathrm{d}t}; \tag{3}$$

$$m_b\frac{\mathrm{d}^2 y}{\mathrm{d}t^2} = p_b\frac{\pi d_b^2}{4} - c_b\left(H_b + y\right) - T_b\mathrm{sign}\frac{\mathrm{d}y}{\mathrm{d}t} - R_b y - \frac{\pi p v_k d_b l_b}{\varepsilon_0}\cdot\frac{\mathrm{d}y}{\mathrm{d}t}; \tag{4}$$

$$\begin{aligned}Q_n - k_n p_n &= c_1 + c_2 f_g(h) + c_3 f_g^2(h) + c_4 p_n + \\ &+\pi d_g z\sin\frac{\alpha_p}{2}\sqrt{\frac{2\left(p_n - p_0\right)}{\rho}}\mathrm{sign}\left(p_n - p_0\right) + \beta W_n\frac{\mathrm{d}p_n}{\mathrm{d}t};\end{aligned} \tag{5}$$

$$c_1 + c_2 f_g(h) + c_3 f_g^2(h) + c_4 p_c F_c v + \beta W_c\frac{\mathrm{d}p_c}{\mathrm{d}t}; \tag{6}$$

$$\pi d_g z \sin\frac{\alpha_p}{2}\sqrt{\frac{2\left(p_n-p_0\right)}{\rho}}\operatorname{sign}\left(p_n-p_0\right)=\mu f_0\sqrt{\frac{2p_0}{\rho}}+ \\ +\beta W_0\frac{\mathrm{d}p_0}{\mathrm{d}t}+\mu f_e\sqrt{\frac{2\left(p_0-p_e\right)}{\rho}}; \tag{7}$$

$$\mu f_e\sqrt{\frac{2\left(p_0-p_e\right)}{\rho}}\operatorname{sign}\left(p_0-p_e\right)= \\ =\beta W_e\frac{\mathrm{d}p_e}{\mathrm{d}t}+\frac{\pi d_4\varepsilon_4^3 p_e}{12\nu_k\rho\left(l_4-l\sin\gamma\right)}-f_4 l\frac{\mathrm{d}\gamma}{\mathrm{d}t}\cos\gamma\operatorname{sign}\frac{\mathrm{d}\gamma}{\mathrm{d}t}; \tag{8}$$

$$\mu f_b\sqrt{\frac{2\left(p_p-p_b\right)}{\rho}}\operatorname{sign}\left(p_p-p_b\right)=\frac{\pi d_b^2}{4}\cdot\frac{\mathrm{d}y}{\mathrm{d}t}+\frac{\pi d_b\varepsilon_b^3 p_e}{12\nu_k\rho\left(l_b-y\right)}+\beta W_b\frac{\mathrm{d}p_b}{\mathrm{d}t}; \tag{9}$$

$$vF_p=\mu\pi d_b\sin\alpha y\sqrt{\frac{2p_p}{\rho}}+\beta W_p\frac{\mathrm{d}p_p}{\mathrm{d}t}; \tag{10}$$

$$i_p F_{NN}=L_e\frac{\mathrm{d}i_m}{\mathrm{d}t}+i_m R_e-k_a\frac{\mathrm{d}z}{\mathrm{d}t}; \tag{11}$$

$$p_c k_c=i_p; \tag{12}$$

$$Q_n=\frac{\pi d_7^2}{4}d_8 k_2 n_n \operatorname{tg}\gamma; \tag{13}$$

$$\beta=\begin{cases}2\times10^{-9}\left(1-0.3\dfrac{p_k}{10^5}\right) & \text{for } p_k\le 23\times10^5, \\ 0.6\times10^{-9} \text{ for } 23\times10^5<p_k\le300\times10^5. & \end{cases} \tag{14}$$

In the mathematical model the following designations are adopted: Q_n is the flow rate of pump *1*; p_c, p_p, p_n, p_0, p_b, p_e – pressures at the input and output of hydraulic cylinder *4*, at the output of pump, in the control system of pump *1*, at the input of pressure compensator *7*, at the input of the pump servocylinder, of the throttle in the pump servocylinder; z – coordinate of the spool position in regulator *2*; v– motion speed of the piston in hydraulic cylinder

4; y – position coordinate of the spool in pressure compensator *7*; γ – rotation angle of the faceplate of variable pump *1*; f_e, f_{gr}, f_0 – areas of the throttle in the pump servocylinder, of the working ports in directional control valve *3* and of the throttle in the pump control system; F_c, F_p, f_4, f_5, F_b – areas of the pistons in hydraulic cylinder *4*, servocylinders of the variable pump and dampers of the pressure compensator; D_c, d_m, d_b, d_7, d_7, d_g – diameters of the hydraulic cylinder *4*, of the spool in regulator *2*, of the pressure compensator spool, variable pump pistons and area of the pump pistons contact with the faceplate, of the pump regulator throttle; k_q, k_m, k_n, k_a, k_c, k_2 – coefficients of the specific friction force in hydraulic cylinder *4*, of the electromagnet proportionality in regulator *2*, of the leakage in pump *1*, of the electromagnet counteraction e.m.f., gain of pressure sensor *10*, the number of pistons in pump *1*; L_e, R_e – inductance and active resistance of the electromagnet windings in regulator *2* and hydraulic cylinder *4*; n_n – rotation speed of the shaft of pump *1*; q_0 – specific force of friction in hydraulic cylinder *4*; ν_k – kinematic viscosity coefficient; ε_p, ε_n, ε_b – clearances between the spool of regulator *2*, servoplunger of pump *1*, the spool of pressure compensator *7* and the bodies; $f_g(h)$ – opening area of the working port in the proportional directional control valve *3*; α_p – inclination angle of the spool in regulator *2*; F_{NN} – transfer function of the neural network; H_b – initial compression of the spring of pressure compensator *7*; R_b – coefficient of hydrodynamic force at the spool of pressure compensator *7*; α – inclination angle of the spool working edge in pressure compensator *7*; c_b – stiffness of the spring in pressure compensator *7*; c_1, c_2, c_3, c_4 – flow rate coefficients of the directional control valve; U_e – voltage supplied to the electromagnet windings; N, T_b – forces of the load at the rod and in pressure compensator *7*; μ – coefficient of flow through the throttling and spool elements; ρ – density of the working fluid; l_p, l_4, l_b, l – lengths of the contact of spool in regulator *2*, servocylinder of pump *1*, spool of pressure compensator *7* with the bodies, the arm of action of servocylinder in variable pump *1*; β – coefficient taking into account total deformation of the working fluid and rubber-metal sleeves; I – inertia moment of the pump faceplate; m_p, m_b, m_c – masses of the spools in regulator and pressure compensator *7*, reduced mass of the working mechanism; W_b, W_n, W_0, W_c – volumes of the hydraulic lines between pump *1* and directional control valve *3*, between regulator *2* and servocylinder *10*, directional control valve *3* and hydraulic cylinder *4*.

Equations of the mathematical model are solved in MATLAB-Simulink software environment (Черных, 2003). As a result of solving the mathematical model equations, dependences of the variables have been obtained. They describe the mechatronic hydraulic system state depending on time for stepwise changes of load N at hydraulic cylinder *4*. From the dependence of pressure p_n at the pump output on time regulation time t_p in the hydraulic system was determined. Regulation time t_p was determined as the moment when variable p_n

enters ±5% corridor relative to steady-state value of the variable. In the mechatronic hydraulic system of hydraulic manipulator the requirements are set to the value of regulation time t_p concerning its restriction to $t_p \leq 0.25$s for the load variation range of $N = (0 - 10) \times 10^3$ N and the mass of moving load to $m_c = 500$ kg. Regulation time t_p in the mechatronic hydraulic system depends, to a great extent, on the combination of design parameters. With the application of the method of genetic algorithm optimal combination of the design parameters for the mechatronic hydraulic system has been found, which provides fulfillment of the regulation time requirements. Table 1 presents the parameters that were changed during optimization process, their variation ranges and the encoded genotypes of the parameters.

Function

$$F(ch_i) = 1 - t_p$$

was used as a chromosome fitness function.

Table 1

Encoding of the Mechatronic Hydraulic System Parameters

Genotype			Phenotype		
			α_p, [degrees]	$f_0 \otimes 10^{-6}$, [m^2]	$f_e \otimes 10^{-6}$, [m^2]
000	000	000	60	0.8	1.5
001	001	001	70	1.0	1.8
010	010	010	80	1.2	2.1
011	011	011	90	1.4	2.4
100	100	100	100	1.6	2.7
101	101	101	110	1.8	3.0
110	110	110	115	2.0	3.3
111	111	111	120	2.2	3.6

During the optimization process maximum of $F(ch_i)$ function must be found while each of the following three parameters is being changed at eight levels: α_p – inclination angle of the working edge of the pump regulator spool, f_0 – throttle areas of the pump regulator, f_e – throttle areas of the pump servocylinder.

Using a random sequence, an output population from 8 chromosomes was formed. The output population is presented in Table 2. 8 numerical experiments were conducted in order to determine fitness function $F(ch_i)$ for each chromosome presented in Table 2. Probability of selection of the chromosomes is determined by the formula

$$P_s(ch_i) = \frac{F(ch_i)}{\sum_{i=1}^{8} F(ch_i)}.$$

Table 2
Initial Population

№ of the chromosome	Genotype	Fitness function $F(ch_i)$	Probability of the chromosome $P_s(ch_i)$ selection
ch_1	001 110 101	0.69	19.4
ch_2	010 100 100	0.65	18.3
ch_3	101 010 101	0.56	15.7
ch_4	101 000 111	0.25	6.9
ch_5	110 000 000	0.47	13.1
ch_6	111 001 111	0.21	5.8
ch_7	111 010 110	0.44	12.2
ch_8	101 000 111	0.31	8.6

From 8 chromosomes, for which fitness functions are determined, three pairs of chromosomes, forming a parental population, have been selected. To the parental population genetic operators were applied. The probability of mutation was taken $p_m = 0$.

Crossover of the chromosomes was performed for locus $L = 2$. Table 3 presents the results of crossover operator application to the parental population, as a result of which population of the first-generation descendants has been obtained.

Table 3
Crossover of the Chromosomes of Parental Population.

Parental population		First-generation descendants	
Chromosome	Fitness function	Chromosome	Fitness function
ch_1 [001 110.101]	0.69	ch_9 [001 110.100]	0.71
ch_2 [010 100.100]	0.65	ch_{10} [010 100.100]	0.63
ch_3 [101 010.101]	0.56	ch_{11} [101 010.110]	0.55
ch_7 [111 010.110]	0.47	ch_{12} [110 000.101]	0.47
ch_7 [111 010.110]	0.44	ch_{13} [111 010.111]	0.37
ch_8 [101 000.111]	0.31	ch_{14} [101 000 110]	0.48

The highest fitness function was calculated for ch_g chromosome $F(ch_i)$= 0.71, which corresponds to the regulation time $t_p = 0.29$ s. Therefore, at the given stage the optimization goal was not achieved. From the first-generation descendents a parental population was formed and, respectively, after cross-over the second-generation descendants were obtained. As a result of selection, after 12 populations chromosome ch_{76} was obtained, which provides accomplishing of the task: regulation time in the mechatronic hydraulic system has been reduced to $t_p = 0.22$ s < $t_c = 0.25$ s. Table 4 presents the optimal combination of the design parameters for the mechatronic hydraulic system.

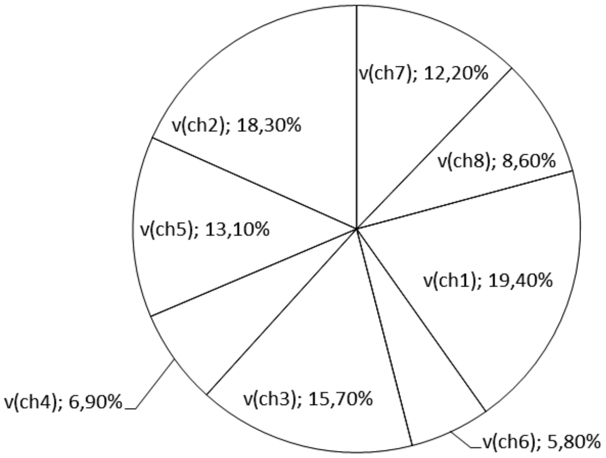

Fig. 2 – Roulette wheel for the initial population of chromosomes.

Table 4

Optimal Values of the Design Parameters of the Mechatronic Hydraulic System.

№ п/п	Parameters	Value
1.	Inclination angle of the working edge of the pump regulator spool	$\alpha_p = 70°$
2.	The pump regulator throttle area	$f_0 = 1.8 \times 10^{-6}$ m^2
3.	The pump servocylinder throttle area	$f_e = 2.4 \times 10^{-6}$ m^2

Conclusion

Application of the genetic algorithm has made it possible to determine the optimal combination of the design parameters for the mechatronic hydraulic system: $\alpha_p = 70°$, $f_0 = 1.8 \times 10^{-6}$ m^2, $f_e = 2.4 \times 10^{-6}$ m^2 which provides regulation time $t_p = 0.22$ s.

REFERENCES

Козлов Л., *Мехатронна гідросистема мобільної машини*. Вісник Східноукраїнського національного університету імені Володимира Даля. – 2012. – №6, С 22-30.

Черных И.В., *Simulink: среда создания инженерных приложений*, М.: Диалог. 2003. – 236 с.

Рутковская Д., Пилинськиий М., Рутковский Л., *Нейронные сети, генетические алгоритмы и нечеткие системы,* – М.: Горячая линия – Телеком, 2006. – 383c.

OPTIMIZAREA PARAMETRILOR SISTEMULUI HIDRAULIC MECATRONIC PRIN METODA ALGORITMULUI GENERIC

(Rezumat)

Manipulatoarele hidraulice sunt utilizate din ce în ce mai mult în industria modernă. Acestea sunt echipate cu dispozitive de apucare cu diferite scopuri. Funcționarea lor este caracterizată de frecvente modificări ale modului de mişcare. În aceste condiții sistemul hidraulic trebuie să asigure minimizarea consumului de energie în timpul ciclului activ cât şi caracteristicvile dinamice şi statice cerute.

Se prezintă un sistem hidraului mecatronic pentru un manipulator care a fost proiectat la Universitatea Tehnică de Stat din Vinița, Ucraina. Sistemul mecatronic include o pompă variabilă cu regulator, o supapă de control direcțional proporțional, un cilindru hidraulic cu piston, un rezervor, un compensator de presiune, un controler, senzori de deplasare şi un senzor de presiune. Controlerul funcționează ca regulator digital in sistemul mecatronic hidraulic. El include unități logice şi două rețele.

A fost creat un model matematic nelinear al sistemului hidraulic mecatronic. Modelul a fost rulat pe MATLAB-Simulink. Soluția ecuațiilor modelului matematic face posibilă găsireacaracteristicvilor dinamice şi statice ale sistemului hidraulic.

Pentru optimizarea sistemului hidraulic mecatronic a fost utilizat un algoritm generic. Timpul de reglare a fost considerat drept criteriu de optimizare în timp ce aria droselului din pompă, poziția regulatorului şi a clapetei servocilindrului au fost considerați printre parametri.

Aplicarea algoritmuluio generic a făcut posibilă determinarea combinației optime a parametrilor sistemului mecatronic hidraulic: $\alpha_p = 70°$, $f_0 = 1.8 \times 10^{-6}$ m^2, $f_e = 2.4 \times 10^{-6}$ m^2 care dau un timp de reglare de $t_p = 0.22$ s.